*sustainability*

MDPI

*Article*

# Suitability Analysis and Potential Assessment for Sustainable Photovoltaic Development in Arid and Semi-Arid Regions of China: A Spatial Framework for Land–Energy Synergy

**Chengxiang Wang [1,2,3,†], Zhengyuan Sun [1,2,3,†], Yitong Gao [1,2,3], Shuyu Xie [1,2,3], Yifan Lu [1,2,3], Dong Liu [4] and Qiuli Yang [1,2,3,*]**

1 College of Geography and Remote Sensing Science, Xinjiang University, Urumqi 830046, China; wcx@stu.xju.edu.cn (C.W.); 15836409511@163.com (Z.S.)
2 Xinjiang Key Laboratory of Oasis Ecology, Xinjiang University, Urumqi 830046, China
3 Xinjiang Field Scientific Observation and Research Station for the Oasisization Process in the Hinterland of the Taklamakan Desert, Yutian 848400, China
4 Desert-Oasis Ecological Monitoring and Restoration Engineering Technology Innovation Center, Xinjiang Uyghur Autonomous Region Land Comprehensive Improvement Center, Urumqi 830063, China
* Correspondence: yangqiuli@xju.edu.cn
† These authors contributed equally to this work.

**Abstract**

Driven by the rapid expansion of the new energy industry and the growing demand for photovoltaic (PV) power plant construction, optimizing site selection to ensure operational efficiency and stability has emerged as a critical imperative. Addressing the lack of precise zonation assessment systems for PV development in China's arid and semi-arid regions, this study introduces a multi-dimensional, five-tier suitability evaluation framework. By integrating Boolean logic, the Bayesian Best–Worst Method (B-BWM), and Equal Interval classification, we developed a multi-resolution integrated assessment framework where spatial boundaries are mainly constrained by 30 m topographic and land-cover data. Results indicate that the candidate PV construction space (the upper two suitability classes, PDSI $\geq$ 3.40) spans 0.85 million km$^2$ concentrated in central-western Inner Mongolia and southeastern Xinjiang, and model validation achieves an Area Under the Curve (AUC) of 0.79. The annual technical potential reaches 19,069 TWh, equivalent to approximately 207% of China's total electricity consumption in 2023. If fully developed, this potential offers a theoretical annual $CO_2$ emission reduction ranging from 12.69 to 21.48 billion tons under different conversion efficiency scenarios, with a baseline estimate of 14.65 billion tons. These multi-resolution integrated findings provide a useful spatial reference for preliminary site screening in arid and semi-arid regions, support China's "Dual Carbon" goals, and offer a practical methodological approach for renewable energy planning on marginal lands.

**Keywords:** sustainable development; sustainable energy transition; photovoltaic site suitability; spatial decision-making tool; land–energy synergy; arid and semi-arid regions



Academic Editor: Maria Malvoni

Received: 4 July 2026
Revised: 31 July 2026
Accepted: 7 August 2026
Published: 11 August 2026



## 1. Introduction

In recent years, accelerated economic growth, urbanization, and industrialization have significantly intensified energy consumption, exacerbating $CO_2$ emissions and the global greenhouse effect [1]. As the world's largest industrial economy and a major emitter, China has committed to a "Dual Carbon" strategy—aiming for a carbon peak by 2030 and carbon neutrality by 2060 [2]. This transition necessitates the aggressive development of renewables, including solar, wind, and tidal energy. Among these, PV power generation has emerged as a pivotal sector due to its high deployment flexibility, suitability for large-scale integration on marginal lands, low operation and maintenance (O&M) costs, and extended operational lifespan [3]. Given that over 50% of global climate finance is currently channeled into renewable energy and grid infrastructure [4], there is an imperative urgency for China to expedite the construction of large-scale PV stations in desert and Gobi regions [5]. The vast solar potential inherent in China's arid and semi-arid zones provides a strategic geographic advantage for the large-scale expansion of PV infrastructure.

China possesses superior solar resource endowment, characterized by extensive spatial distribution and significant development potential. In 2023, the national average Global Horizontal Irradiance (GHI) reached 1496.1 kWh/m$^2$ [6], with high-potential regions such as Tibet and Qinghai exceeding 1700 kWh/m$^2$ [7]. By the end of 2023, China's cumulative grid-connected PV capacity reached 608.92 GW [7], reinforcing its global leadership in the sector. Concurrently, solar power generation surged to 583.3 TWh [8]—a profound 36.4% year-on-year increase—accounting for 6.3% of the national total. This trajectory underscores the robust momentum behind the green transformation and decarbonization of China's power system.

Methodological frameworks for global multi-scale PV suitability assessment are increasingly anchored in Multi-Criteria Decision-Making (MCDM), with significant advancements in algorithmic innovation, model coupling, and scenario diversification. To enhance weighting robustness and manage uncertainty, recent research has orchestrated a multi-criteria weight aggregation and refined spatial mapping framework by coupling the B-BWM with Weighted Linear Combination (WLC) algorithms [9]. By integrating high-resolution spatial datasets, this approach effectively mitigates subjective bias in site selection for high-altitude and ecologically fragile regions. Regarding regional energy synergy, the optimization of evaluation indices—through the integration of AHP-TOPSIS and multicollinearity diagnostics—combined with ARIMA-based dynamic demand forecasting has achieved a deep coupling between PV potential and regional load requirements [10]. To sharpen spatial constraint logic, hybrid fuzzy–Boolean logic has been introduced; Boolean operators strictly exclude restricted zones (such as ecologically sensitive or land-use-constrained areas), while fuzzy logic addresses boundary ambiguity, thereby ensuring logical consistency and scientific rigor [11]. Furthermore, the evaluative scope has expanded from terrestrial systems to integrated assessments of land-based and Floating PV (FPV). Some studies have also employed Structural Equation Modeling (SEM) to elucidate the latent structural interrelationships among influencing factors, further enriching the theoretical and practical dimensions of PV suitability research [12].

Despite the robust foundation established by the existing literature, critical research gaps persist regarding regional precision, data fidelity, and framework specificity, which constrain the practical efficacy of current models. First, most studies are confined to administrative boundaries (e.g., national or provincial scales) [10,13], leaving a paucity of systematic research on distinct biogeographical and climatic zones, such as arid and semi-arid regions. This neglect fails to reconcile the dual characteristics of superior solar endowment versus extreme ecological fragility, thereby failing to support the precise spatial deployment of PV infrastructure at a regional scale. Second, the lack of spatial resolution—with many studies relying on 1 km or coarser data—leads to a smoothing effect. This obscures critical micro-topographical variations, small-scale infrastructure, and fragmented marginal lands, resulting in low spatial accuracy that cannot meet the requirements for fine-grained site selection in massive desert and Gobi PV stations [11]. Third, existing evaluation frameworks often lack regional specificity, relying on generic

https://doi.org/10.3390/su18168218

indicators that overlook the unique constraints of arid environments, such as scarce precipitation, poor surface stability, and homogeneous land use. The insufficient integration of key regional constraints, particularly the synergistic management of ecological redlines and marginal lands, leads to a misalignment between assessment results and local realities [10,12,13]. Fourth, subjective uncertainty in weight determination remains a challenge. Although methods like B-BWM have improved objectivity, the weighting synergy mechanisms and sensitivity analyses concerning complex trade-offs (e.g., ecological sensitivity vs. resource abundance) remain underdeveloped, potentially jeopardizing the reliability of the evaluation models [9].

To address these gaps, the primary contribution of this study lies in its regional application and context-specific indicator configuration tailored for the climatic boundary of China's arid and semi-arid regions [14]. By adapting established multi-criteria decision-making (MCDM) methods to this specific environment—such as configuring non-monotonic suitability thresholds for temperature to reflect thermal degradation risks—this research provides a refined evaluation framework that balances technical accessibility with ecological preservation. Specifically, this study sets out to answer the following research questions: (1) How can an MCDM framework, driven by regional indicators and multi-resolution spatial constraints, be configured to assess photovoltaic suitability in arid and semi-arid zones while rigorously preserving ecological redlines? [15] (2) To what extent do subjective Bayesian Best–Worst Method (B-BWM) [16] weight perturbations and deterministic Boolean exclusion thresholds influence the spatial distribution and stability of the identified suitable areas? (3) What is the scenario-based technical generation potential and the associated gross theoretical carbon reduction achievable under conservative land-utilization assumptions?

## 2. Materials and Methods

### *2.1. Study Area*

As illustrated in Figure 1, the main map displays the GHI levels throughout the arid and semi-arid regions of China, while the inset map in the bottom-right corner defines the study area relative to the entire country. This research focuses on China's arid and semi-arid regions [14], which serves as a critical ecological safety barrier for Northwest China and East Asia. Geographically, this territory constitutes a pivotal transition zone—or ecotone—among the Eastern Monsoon region, the Northwestern Arid Inland region, and the Qinghai–Tibet Alpine region. Spanning approximately 5.16 million km$^2$ (Figure 1), the area holds indispensable strategic value for maintaining regional climatic stability and ecological equilibrium. Driven by its unique geographic positioning and climatic conditions, the region exhibits superior solar resource endowment. Due to sparse precipitation and high atmospheric transparency, the GHI across most of the area consistently exceeds 1500 kWh/m$^2$ [7]. Combined with vast reserves of marginal land, this region represents the strategic core for China's large-scale PV transition and the realization of "Dual Carbon" goals [2]. However, this high development potential is juxtaposed with extreme ecological sensitivity; conventional extractive development patterns risk destabilizing the fragile surface equilibrium. Consequently, the study area is both a highland for energy production and a frontline for ecological restoration. By identifying complex physiographic constraints, this study aims to transform PV infrastructure from simple resource extraction into an endogenous driver for desertification control and ecological functional recovery. Ultimately, this work explores a scientific pathway for the deep synergy between resource utilization, high-level ecological benefits, and green power output.

https://doi.org/10.3390/su18168218

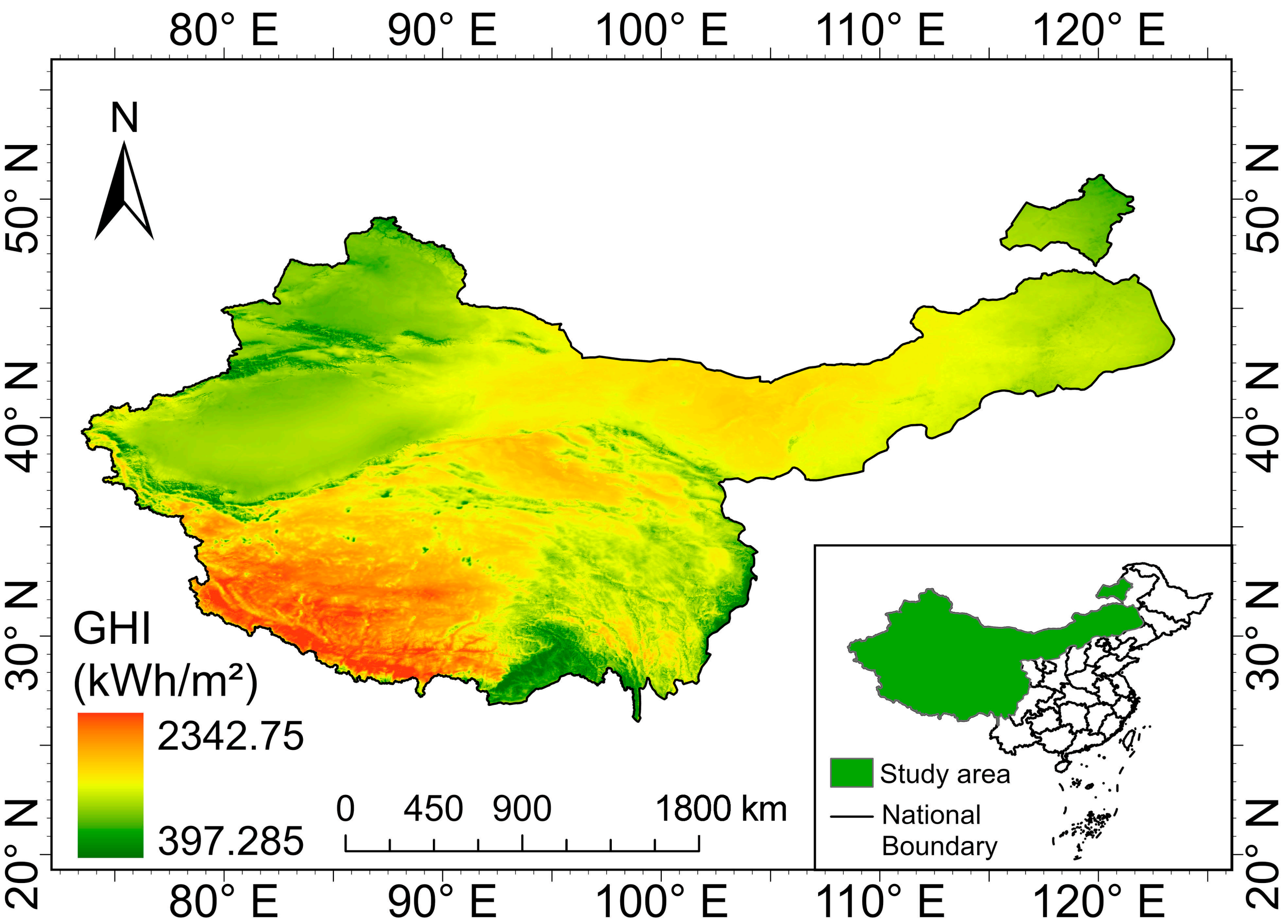


**Figure 1.** Study area and GHI distribution.

### *2.2. Data and Methods*

#### 2.2.1. Data Sources

To support the suitability evaluation of PV development in arid and semi-arid regions, this study integrates multi-dimensional spatial and attribute data, including topographic, climatic, land cover, and location factors. Detailed information is provided in Table 1.

**Table 1.** Characteristics and sources of the multi-dimensional geospatial datasets used for PV suitability assessment.

| **Datasets** | **Unit** | **Spatial Resolution** | **Types** | **Sources** |
|---|---|---|---|---|
| Aspect | ° | 30 m | Raster | SRTMGL1 v3 DEM (2000) from GEE [17] |
| Slope | ° | 30 m | Raster | SRTMGL1 v3 DEM (2000) from GEE [17] |
| Elevation | m | 30 m | Raster | SRTMGL1 v3 DEM (2000) from GEE [17] |
| GHI | kWh/m$^2$ | 1 km | Raster | Global Solar Atlas [18] |
| Temperature | °C | 1 km | Raster | MOD11A2 v6.1 (2023) from GEE [19] |
| Land use | \ | 30 m | Raster | 2020 global 30 m surface coverage fine classification products [20] |
| NDVI | \ | 1 km | Raster | MOD13A3 MODIS/Terra vegetation Indices [20] |
| Nature Reserve | \ | \ | Vector | Open Street Map (https://www.openstreetmap.org/) [21] |
| Roads | \ | \ | Vector | Open Street Map (https://www.openstreetmap.org/) [21] |

https://doi.org/10.3390/su18168218

**Table 1.** *Cont.*

| Datasets | Unit | Spatial Resolution | Types | Sources |
|---|---|---|---|---|
| Railways | \ | \ | Vector | Open Street Map (https://www.openstreetmap.org/) [21] |
| Powerlines | \ | \ | Vector | Arderne, C., Zorn, C., Nicolas, C. et al. [22] |
| Water Bodies and Wetlands | \ | \ | Vector | Open Street Map (https://www.openstreetmap.org/) [21] |
| Farmlands and Forests | \ | \ | Vector | Open Street Map (https://www.openstreetmap.org/) [21] |
| PV Sites | \ | \ | Vector | Gao Y, Yang Q, Chang P. et al. [23] |
| Settlements | \ | \ | Vector | Han J, Hu Z, Zhou K. et al. [24] |

#### 2.2.2. Topographic Data

Topographic data, comprising elevation, slope, and aspect, were derived from the Shuttle Radar Topography Mission (SRTM) dataset released by the United States Geological Survey (USGS) and extracted via Google Earth Engine (GEE) [17]. This dataset possesses an original spatial resolution of 30 m. Acquired using radar interferometry technology, the SRTM dataset covers the global land surface and is widely utilized in detailed topographic analysis with validated accuracy. Consequently, it accurately captures the topographic relief characteristics of the study area, providing foundational support for assessing the topographic suitability of PV power station site selection.

#### 2.2.3. Climatic Data

The key climatic indicator, GHI, was sourced from the Global Solar Atlas with a spatial resolution of 1 km [18]. Generated through the fusion of satellite remote sensing observations and ground-based station data, this dataset effectively mitigates data gaps caused by the sparse distribution of ground stations. It accurately characterizes the spatial distribution patterns of solar resources in arid and semi-arid regions, serving as the core data source for assessing PV development potential. Furthermore, land surface temperature (LST) data were acquired from the MOD11A2 (Collection 6.1) product via the GEE platform [19]. Specifically, the daytime LST variable (LST_Day_1 km) was extracted and temporally aggregated to calculate the annual mean temperature for 2023, serving to delineate the environmental thermal conditions for PV module operation.

#### 2.2.4. Land Cover Data

Land use data were derived from the 2020 global 30 m surface coverage fine classification products released by the National Geomatics Center of China (NGCC) [25], with a spatial resolution of 30 m. This data set encompasses 29 land cover types and achieves a classification accuracy exceeding 85%, thereby satisfying the requirements for regional-scale land use characterization. It was utilized to explicitly delineate the land areas suitable for PV development, while also serving as a basis for identifying ecological constraint factors.

The Normalized Difference Vegetation Index (NDVI) data were derived from the MOD13A3 dataset, comprising both monthly NDVI raster data and annual mean NDVI raster calculated by averaging the monthly series [20]. With a spatial resolution of 1 km, this dataset effectively reflects surface vegetation coverage, particularly in the arid and semi-arid regions of China, which are characterized by relatively homogeneous land use types.

#### 2.2.5. Location Data

This study incorporates two core categories of spatial information regarding infrastructure and ecological constraints. Specifically, power grid distribution data were sourced from the OpenStreetMap (OSM) database [21] and the predictive dataset developed by Arderne et al. [22], based on OSM. Additionally, road and railway network data were derived from the OSM database and accessed via the GEE platform [17,21].

#### 2.2.6. Other Data

Other supplementary datasets were also utilized. Ecological constraint data (e.g., nature reserves and wetlands) were obtained from OSM [21] to identify and avoid ecologically sensitive areas, ensuring a balance between energy development and environmental protection. Settlement data were derived from the high-accuracy (90.19%) dataset published by Prof. Hu Zhenqi's team at China University of Mining and Technology (CUMT) on the Science Data Bank [24]. Furthermore, to validate the model's accuracy, PV site data were adopted from the 2023 dataset by Gao et al. [23], which encompasses the precise coordinates of more than 90% of China's PV stations.

#### 2.2.7. Data Preprocessing

All datasets were reprojected to the Albers Equal Area Conic projection based on the CGCS2000 datum, China Geodetic Coordinate System 2000, to minimize areal distortion during distance buffering and spatial computations. To address discrepancies in resolution, data with lower native resolutions were resampled to 30 m using the nearest neighbor interpolation method for categorical data (e.g., land use) and bilinear interpolation for continuous variables. It should be noted that while this standardizes the analytical grid size, it does not artificially increase the actual information content of the native 1 km climate and vegetation datasets. Therefore, the final assessment represents an integrated suitability zoning primarily constrained and driven by the 30 m land-cover and topographic spatial boundaries, ensuring high spatial consistency for subsequent analysis.

During the resampling process, the 30 m land use raster was designated as the snap raster to ensure perfect cell alignment across all layers. Any NoData values in the input layers were masked out and excluded from the spatial integration.

### *2.3. Methodological Framework*

A methodological framework was constructed to delineate PV priority areas and assess the development potential in the arid and semi-arid regions of China (Figure 2). This framework consists of the following five steps:

(1) The necessary geospatial data were acquired to establish the suitability criteria and constraint indicators governing PV site selection.
(2) We excluded unsuitable regions to identify the potential area.
(3) Weights for the suitability indicators were determined using the B-BWM [16], followed by the categorization of each indicator into five levels.
(4) The WLC method [26] was implemented in ArcGIS Pro 3.3.4 (Esri, Redlands, CA, USA) to calculate the suitability index. The results were then clipped to the Potential area defined in Step (2) and classified into five grades using the Equal Interval classification, ultimately generating the PV suitability map.
(5) The top two suitability levels were extracted to define suitable areas for PV development. Following an accurate assessment via the Receiver Operating Characteristic Curve (ROC) [27], the potentials for power generation and carbon abatement were derived based on the established formulas.

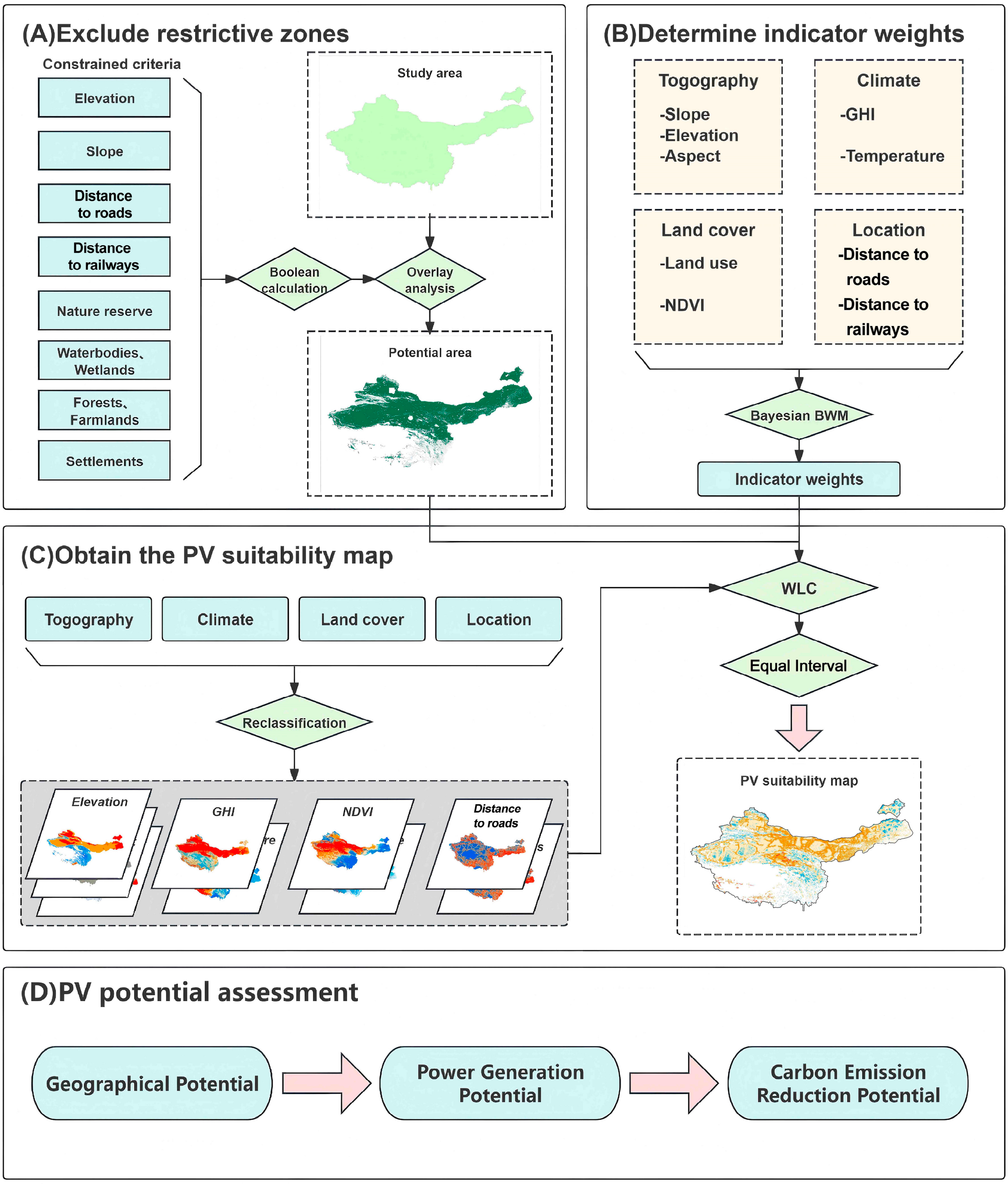


**Figure 2.** Integrated spatial decision-making framework for regional photovoltaic suitability and environmental-energy synergy assessment. Colors within the flowchart are utilized solely for aesthetic purposes to visually distinguish the structural modules, and do not represent specific categorical data types.

## *2.4. Assessment Framework*

### 2.4.1. Restrictive Factors

The site selection for PV power stations requires balancing economic benefits with construction costs while strictly adhering to national laws and regulations [28–30] and satisfying the requirements of nature conservation. Incorporating limitations on various factors identified in prior research [9,10] and considering the regional characteristics of China's arid and semi-arid areas, this study identified and excluded 10 restrictive indicators (Table 2). The spatial distribution of these indicators is illustrated in Figure 3.

**Table 2.** Restriction area and the conditions.

| Criteria | Restriction Conditions |
|---|---|
| Nature Reserves | The areas where nature reserves are |
| Elevation | The areas with elevation greater than 4500 m |
| Water bodies | The areas where they are |
| Roads | Areas within 100 m of roads |
| Settlements | The areas where settlements are |
| Slope | Areas with a slope greater than 20° |
| Farmlands | The areas where they are |
| Wetlands | The areas where they are |
| Railways | Areas within 100 m of railways |
| Closed-canopy Forests | The areas where they are |

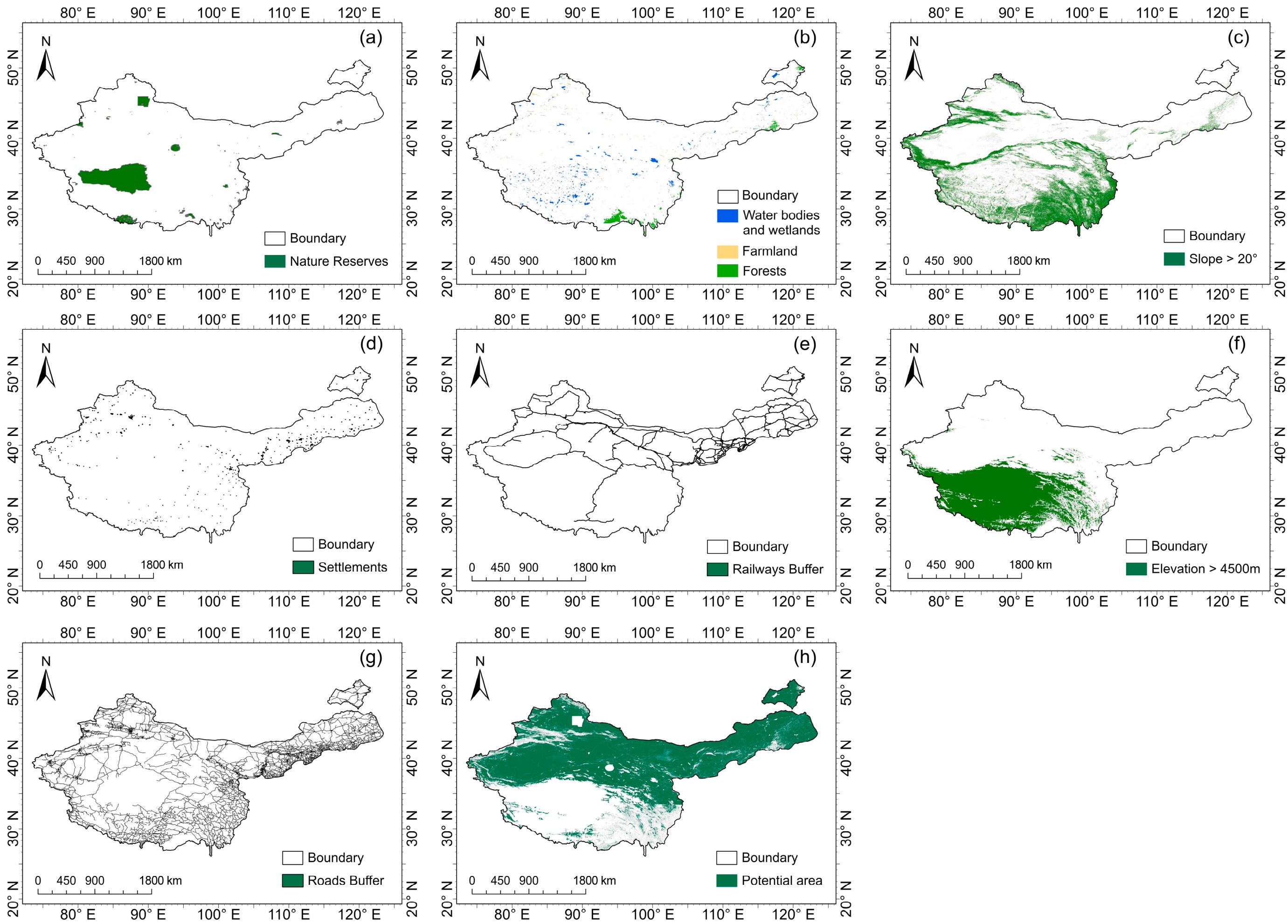


**Figure 3.** Spatial distribution of restrictive factors and the resulting potential area. Subfigures (**a**) nature reserves; (**b**) farmland, forests, waterbodies, and wetlands; (**c**) slope; (**d**) settlements; (**e**) railways buffer; (**f**) elevation; (**g**) roads buffer; (**h**) potential area: the area excluding restricted zones.

(1) Construction difficulty. Terrain conditions directly influence the construction difficulty, cost, and subsequent operational efficiency of PV power stations. Therefore, following PV construction standards (GB 50797-2012) [31] and widely accepted engineering criteria [9,10], this study excluded areas with an elevation greater than 4500 m (where severe equipment derating occurs) [32] and a slope greater than 20° [33] (which drastically increases civil engineering costs and inter-row shading).

(2) Traffic factors. For major roads [34] and railways [35], constructing PV power stations in close proximity may pose traffic safety risks and hinder future expansion and maintenance of the infrastructure. Consequently, a 100 m buffer zone was established along roads and railways and excluded from the study to comply with transportation safety regulations [34,35] and to mitigate the risks of PV panel glare on drivers. Simultaneously, considering the land use nature of towns and rural settlements and their compatibility issues with large-scale PV power stations, this study excluded residential settlements and urban construction land from the candidate areas [36].

(3) Environmental protection. In compliance with national ecological protection red lines and relevant laws and regulations [28–30], this study strictly excluded ecologically extremely sensitive areas such as nature reserves, water bodies, and wetlands. Furthermore, to effectively implement the cultivated land red line protection policy [37] and maintain forest ecosystem functions, closed-canopy forests and farmlands (serving as a spatial proxy for arable land protection redlines) were completely masked out as prohibited development zones, whereas open forests and sparse shrublands were retained for further suitability scoring, thereby achieving a balance between energy development, ecological carbon sequestration, and food security.

(4) The complete Boolean mask was formalized as a sequential raster calculation: Potential_Mask = (Elevation $\leq$ 4500) AND (Slope $\leq$ 20) AND (Distance to Roads > 100) AND (Distance to Railways > 100) AND NOT (Settlements) AND NOT (Nature Reserves) AND NOT (Water Bodies) AND NOT (Wetlands) AND NOT (Farmlands) AND NOT (Closed Canopy Forests). This expression was executed in ArcGIS Pro using the Raster Calculator tool, which sequentially evaluates each condition on a per-cell basis, assigning a value of 1 to cells satisfying all criteria (potential area) and 0 (NoData) to cells failing any single constraint, thereby generating a binary potential-area mask for subsequent suitability scoring.

#### 2.4.2. Suitability Factors

After excluding the restricted areas, this study selected 9 evaluation indicators from four dimensions: Climate, Topographic, Location, and Land cover. The Climate factors include: GHI (C1) and Temperature (C2); Topographic factors include: Elevation (C3), Slope (C4), and Aspect (C5); Location factors include: Distance to roads (C6) and Distance to transmission lines (C7); and Land cover factors include: Land use type (C8) and NDVI (C9). The classification thresholds and reclassification standards for each indicator are presented in Table S1, and the spatial distribution following reclassification is shown in Figure 4.

(1) Topographic—Elevation: After excluding areas with excessively high elevation, the remaining areas were categorized into five levels of suitability [9,33]. Aspect: Since China's arid and semi-arid regions [14] are located in the Northern Hemisphere, south-facing slopes are more conducive to receiving sunlight, whereas north-facing slopes are situated on the shady side and receive less solar radiation. Slope: Excessively steep slopes significantly increase the difficulty and cost of PV construction; thus, flatter areas are more suitable for the installation of PV panels.

(2) Climate—GHI is a critical factor influencing PV power generation; it directly determines the electrical output of PV panels and is an indispensable component of PV suitability development. Meanwhile, Temperature affects the conversion efficiency of PV panels. Excessively low temperatures can have a negative impact on the lifespan and performance of PV modules; thus, lower temperatures are considered less suitable. Conversely, excessively high temperatures can lead to accelerated aging of PV modules, shortening their service life [38–40].

To accurately reflect this non-monotonic physical mechanism, the suitability scoring was adjusted to penalize extreme thermal conditions. Optimal suitability scores (Level 5) were assigned to moderate temperature zones, while regions exceeding the optimal threshold (e.g., extreme high-temperature areas in the desert basins) received progressively lower scores to account for thermal degradation and efficiency losses.

(3) Land cover—Land use type: The difficulty of constructing PV power stations varies across different land use types. Simultaneously, national policies encourage the construction of PV projects in deserts and Gobi areas; building PV stations in these areas also minimizes the encroachment on arable land [41]. NDVI intuitively reflects the vegetation coverage of each region, facilitating the screening of areas with lower vegetation density for PV development [42].

(4) Location—Being closer to roads facilitates the construction of PV power stations, saving costs on transportation and the construction of new roads [43]. Being closer to transmission lines saves on transmission costs and reduces electricity losses during the transmission process [44].

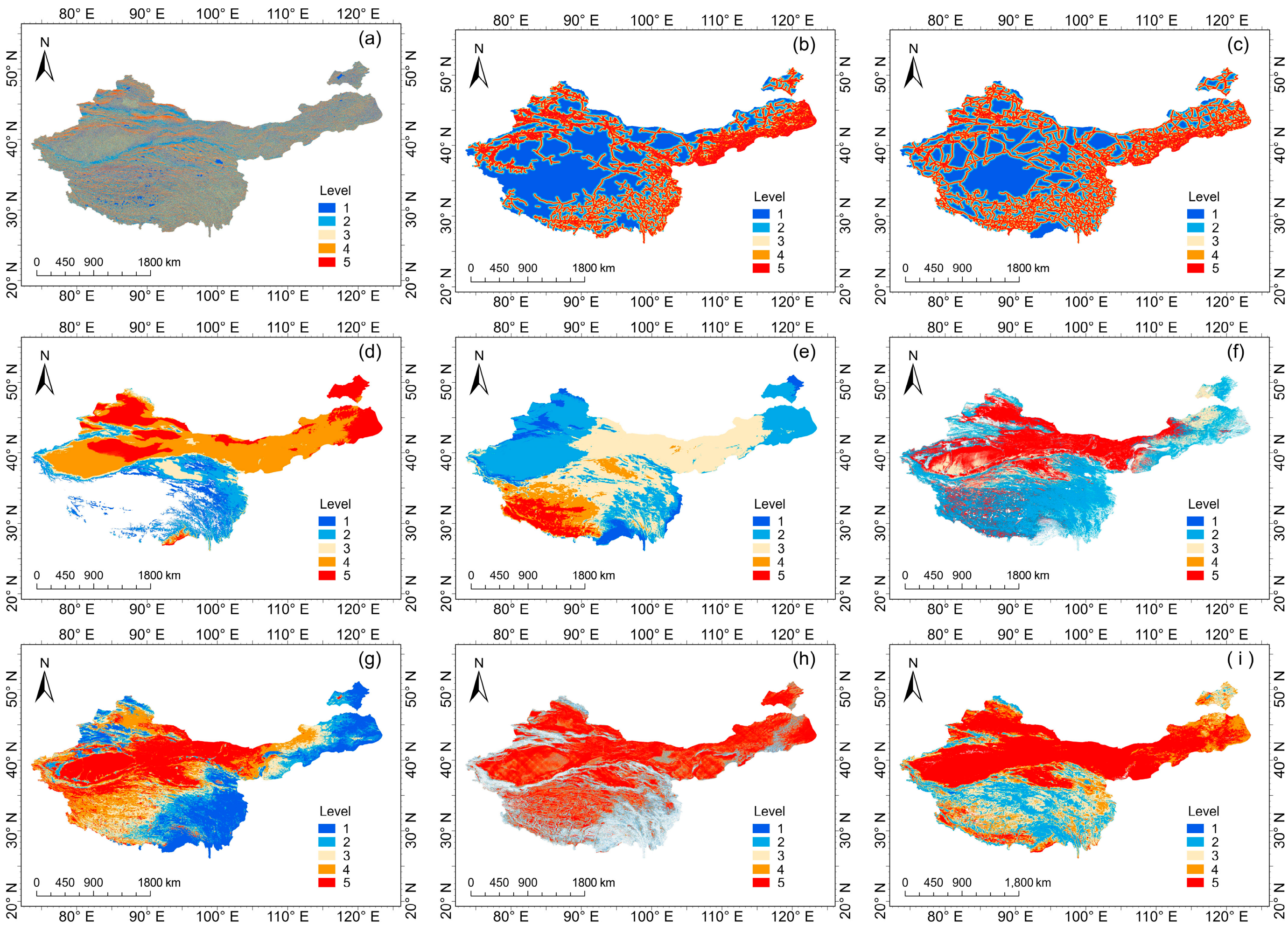


**Figure 4.** Spatial distribution of reclassified suitability indicators within the potential area. The maps illustrate the five-tier suitability grading (Level 1: less suitable to Level 5: highly suitable) for nine criteria: (**a**) aspect; (**b**) distance to powerlines; (**c**) distance to roads; (**d**) elevation; (**e**) GHI; (**f**) land use; (**g**) NDVI; (**h**) slope; (**i**) temperature.

### 2.4.3. Determination of Weights

Currently, numerous mainstream weight assessment methods exist. Among them, the B-BWM [16] integrates subjectivity with objectivity, offering a simple methodology with accurate results. Consequently, it has emerged as a prominent approach for weight assessment in Geographic Information Systems (GIS) in recent years. Compared to traditional MCDM analysis methods, B-BWM can simultaneously determine the optimal weights for all decision-makers (DMs) and the aggregated final weights, thereby minimizing information loss during the group decision-making process to the greatest extent.

The steps of the B-BWM are as follows:

Step 1: Determining a set of decision criteria $C = \{c_1, c_2, c_3, \ldots, c_n\}$ through literature review and expert opinions. $n$ is the number of criteria.

Step 2: Determining the most important criterion $B$ and the least important criterion $W$ from $C$.

Step 3: Pairwise comprising $B$ with other criteria from $C$.

Determining the priority of the best criterion relative to all other criteria using a numerical scale from 1 to 9, where 1 is equal importance and 9 is the highest importance. The vector of best-to-others would be $A_B = (a_{B1}, a_{B2}, a_{B3}, \ldots, a_{Bn})$, where $a_{Bj}$ is the preference of the best criterion $B$ over criteria $j$, and $a_{BB} = 1$.

Step 4: Pairwise comprising $W$ with other criteria from $C$.

Similarly, determining the priority of all criteria over the worst criterion, using a number from 1 to 9. The vector of others-to-worst would be $A_W = (a_{1W}, a_{2W}, a_{3W}, \ldots, a_{nW})^T$, where $a_{jW}$ is the preference of criteria $j$ over the worst criterion $W$, and $a_{WW} = 1$.

Step 5: Computing the optimal weights $w^*$ of single DM.

Solving Equation (1) and the consistency ratio to find the optimal weights $w^* = \{w^*{}_1, w^*{}_2, w^*{}_3, \ldots, w^*{}_n\}$.

$$
\begin{aligned}
&\min \xi \\
&s.t. \\
&\left|\frac{w_B}{w_j} - a_{Bj}\right| \le \xi, \forall j = 1,2,3,\ldots,n \\
&\left|\frac{w_j}{w_W} - a_{jW}\right| \le \xi, \forall j = 1,2,3,\ldots,n \\
&\textstyle\sum_{j=1}^{n} w_j = 1, w_j \ge 0, \forall j = 1,2,3,\ldots,n
\end{aligned} \tag{1}
$$

Step 6: Computing the aggregated weights $w^{agg}$ of multiple DMs.

Calculating the overall preferences of all DMs using the Bayesian hierarchical model to get aggregated weights $w^{agg}$ by Equation (2).

$$
\begin{aligned}
&A_B^n | w^n \sim multinomial(1/w^n), \forall n = 1,2,3,\ldots,N \\
&A_W^n | w^n \sim multinomial(w^n), \forall n = 1,2,3,\ldots,N \\
&w^n | w^{agg} \sim Dir(\gamma \times w^{agg}), \forall n = 1,2,3,\ldots,N \\
&\gamma \sim gamma(a,b), \\
&w^{agg} \sim Dir(\alpha).
\end{aligned} \tag{2}
$$

where *multinomial* is the multinomial. *Dir* is the Dirichlet distribution, $w^{agg}$ is the mean of the distribution, and $\gamma$ is the concentration parameter. gamma represents a gamma distribution, and $a$ and $b$ are form parameters: $a = 0.1$ and $b = 0.1$. $\alpha$ is the parameter of the Dirichlet distribution, and $\alpha = 1$.

### 2.4.4. Integrated Weighting

The WLC method is a weight integration technique widely applied in the field of GIS [26]; therefore, this study adopts this method for suitability assessment. After determining the weights of each evaluation indicator, the WLC algorithm is employed to weigh all indicators and integrate them to calculate the Photovoltaic Development Suitability Index (PDSI) for each grid cell in the study area using Equation (3) [27].

$$PDSI_i = \sum_{j=1}^{n} w_j^{agg} \times c_{ij} \tag{3}$$

where $PDSI_i$ represents the PV suitability index of grid cell $i$, $w_j^{agg}$ denotes the weight value of criterion $j$, and $c_{ij}$ represents the value of grid cell $i$ under criterion $j$.

### *2.5. Potential Assessment*

#### 2.5.1. Geographic Potential

Based on the results derived from the B-BWM method and the WLC calculation described previously, a preliminary PV suitability map was obtained. As this initial map did not differentiate between suitability levels, this study employed the Equal Interval method to classify the results into five levels. The top two levels were selected to represent the geographic potential results, which were then validated for accuracy using data from existing PV power stations in 2023 [23].

To precisely determine the rationality of the PV suitable area classification, this study adopted the ROC method for validation [27].

To construct a robust validation dataset matching the true positive samples, an equal number of pseudo-absence points ($n$ = 2111) were generated through a strictly randomized procedure within the potential area. Specifically, random geographic coordinates were drawn from a uniform distribution across the spatial extent of the non-restricted potential zone, with the constraint that all pseudo-absence points lie at least 1 km away from any existing PV station to avoid spatial autocorrelation. The randomization was implemented using the Mersenne Twister algorithm with a fixed seed to ensure reproducibility. To evaluate the statistical stability of the resulting AUC metric against variability in background sampling, a bootstrap resampling procedure with 2000 iterations was performed: in each iteration, a new set of 2111 pseudo-absence points was independently drawn, and the AUC was recomputed. The final reported AUC represents the mean across all bootstrap iterations, with the 95% confidence interval appended. This approach ensures that the reported model accuracy is not an artifact of a particular random draw but reflects the robust discriminatory power of the PDSI framework.

To ensure transparency in our spatial validation workflow, we explicitly quantify the impact of the Boolean exclusion mask on the existing PV station inventory. Among the total initial inventory of 1923 operational PV stations across the study area, exactly 36 facilities (1.87%) completely overlapped with predefined restricted zones (primarily agricultural farmland, waterbodies, or steep terrain > 20°) and were consequently excluded. These minor exclusions are primarily attributed to temporal discrepancies between the land-use dataset (2020) and PV station records (2023), as well as specialized light-use project types (e.g., agrivoltaics or fishery–solar hybrids) that deviate from utility-scale deployment logic. This low rejection rate (1.87%) serves as an independent check of the Boolean mask, indicating that our exclusion criteria do not systematically omit existing PV locations. Subsequently, the spatial discriminatory capacity of the continuous PDSI scoring model was evaluated independently across the remaining non-restricted candidate space.

The remaining 1887 stations located within the non-restricted potential area were intersected with the potential mask. Due to 154 multi-part facilities spanning across restricted boundaries, this geometric intersection yielded 2252 polygon fragments. After converting these polygons to centroid point features and masking out edge or invalid

NoData pixels at the 30 m grid boundary, a final validated dataset of 2111 true positive centroid sample points was established for ROC/AUC assessment.

To evaluate spatial predictive accuracy, the Receiver Operating Characteristic (ROC) curve and the corresponding Area Under the Curve (AUC) were calculated directly from the continuous PDSI raster scores across all sampled locations. This identical continuous calculation method was consistently applied across the primary validation as well as all subsequent OAT and LOO sensitivity analyses. Specifically, by systematically varying the discrimination threshold across the entire continuous distribution of PDSI scores, the corresponding TP, FN, FP, and TN values were evaluated at each threshold cutoff to compute the True Positive Rate (TPR) and False Positive Rate (FPR) using Equation (4):

$$\begin{aligned} TPR &= TP/(TP + FN) \\ FPR &= FP/(FP + TN) \end{aligned} \tag{4}$$

Subsequently, with FPR as the x-axis and TPR as the y-axis, the paired values across all continuous thresholds were plotted to generate the complete stepped ROC curve. The closer the ROC is to the upper-left corner, the more accurate the prediction result.

Furthermore, the Area Under the Curve (AUC) serves as the core evaluation metric for ROC validation, representing the area between the ROC and the x-axis. Its magnitude directly reflects the precision of the prediction results. It is generally accepted that an AUC below 0.7 indicates poor model prediction capability and insufficient credibility; an AUC between 0.7 and 0.8 indicates good model prediction results with decent credibility; and an AUC exceeding 0.8 represents excellent model prediction capability and higher credibility.

### 2.5.2. Power Generation Potential

Power generation potential can be defined as the quantity of electricity into which solar radiation can be converted, given current solar energy technologies. The power generation potential of a PV system can be calculated using Equation (5) [45]:

$$TPSE = GHI \times EF \times AREA \times PR \tag{5}$$

where TPSE represents the power generation potential of the PV power station (kWh/year), GHI is the solar irradiance value at the PV power station site (kWh/m$^2$/year), EF refers to the efficiency with which the PV system converts solar energy into electrical energy, AREA denotes the available area for PV power station installation (m$^2$), and PR indicates the performance ratio of the PV modules.

It should be noted that using Global Horizontal Irradiance (GHI) directly, rather than Plane-of-Array (POA) irradiation, represents a methodological simplification to provide a conservative, first-order screening estimate of solar potential.

The value of EF is constrained by the materials and processes used in the PV system. Current PV systems predominantly utilize monocrystalline silicon, polycrystalline silicon, and gallium arsenide (GaAs) cells. Among these, monocrystalline silicon is the most widely applied material, occupying an 80% market share. The EF of monocrystalline silicon materials ranges between 13% and 22% [46–48]; this study conservatively adopts 15% as the EF value. Furthermore, considering that conversion efficiencies vary across different systems and materials, as well as the constraints of economic costs and future updates in conversion efficiency, this study also performed power generation potential calculations for EF values of 13% and 22% to conduct a sensitivity analysis. The value of PR typically ranges from 70% to 85% [49]; this study conservatively adopts 70%.

2.5.3. Carbon Emission Reduction Potential

Carbon emission reduction potential refers to the quantity of carbon emissions that can be mitigated by substituting thermal power generation with PV power generation, assuming equivalent electricity output. It can be quantified as the theoretical carbon emissions associated with the coal consumption required to produce the same amount of electricity via thermal power generation as that generated by PV systems. Based on the estimated power generation potential and Equation (6) [50], the carbon emission reduction potential is projected as follows:

$$CE = b \times TPSE \times C \quad (6)$$

where CE represents the carbon emission reduction ($tCO_2$), b denotes the standard coal consumption for power generation (g/kWh), and C signifies the $CO_2$ emissions produced by the combustion of one ton of standard coal. According to the "2021 Electric Power Industry Statistical Yearbook" [51], the national average coal consumption for power supply, b, is 302.5 g/kWh, and the specific value of C is 2.54 (t $CO_2$ per tonne of standard coal).

To ensure rigorous order-of-magnitude accuracy in the final calculation, the raw output is divided by $10^6$ to convert the mass of carbon emissions from grams to metric tons (t $CO_2$).

## 3. Results

*3.1. Mapping of PV Priority Areas*

Upon obtaining the results from Section 2.4.3 (Table S2), this study utilized the Equal Interval method to categorize the study area into five suitability levels: less suitable (1.0–1.8), marginally suitable (1.8–2.6), moderately suitable (2.6–3.4), suitable (3.4–4.2), and highly suitable (4.2–5.0). The spatial distribution and area proportions are detailed in Figure 5.

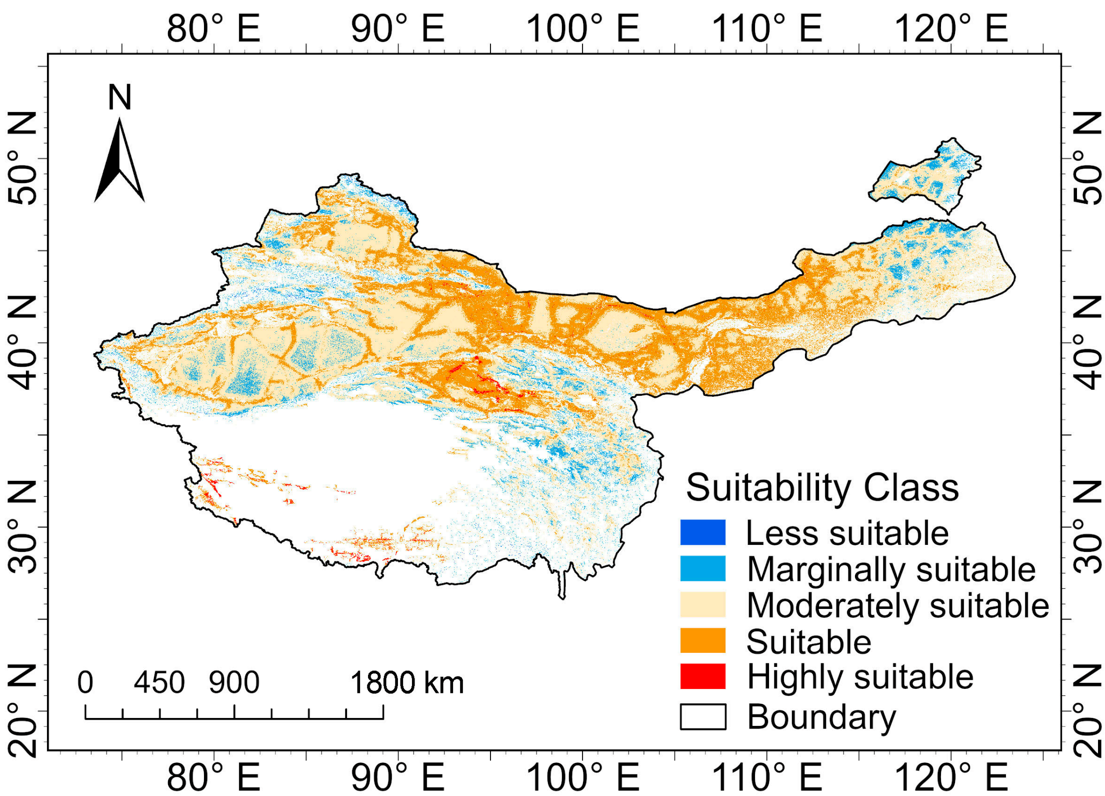


**Figure 5.** Grade-classified suitability areas.

The results indicate that the upper two suitability classes (PDSI $\geq$ 3.40, comprising the suitable and highly suitable zones) account for 32.29% and 0.83% of the potential area, respectively (Table 3), together defining the baseline geographic potential area. In terms of spatial distribution, the highly suitable areas are primarily concentrated in central and western Inner Mongolia as well as southern and eastern Xinjiang. Notably, approximately one-third of the area in Inner Mongolia is designated as suitable or above, identifying it as the province with the greatest potential for PV development within the arid and semi-arid regions. Furthermore, Xinjiang also possesses large contiguous areas classified as highly suitable and suitable, similarly rendering it highly favorable for PV development.

**Table 3.** Area and percentage distribution of PV suitability classes based on the Equal Interval method.

| Suitability Class | Area (km$^2$) | % of Total Study Area | % of Potential Area |
|---|---|---|---|
| Highly suitable | 21,268 | 0.41% | 0.83% |
| Suitable | 827,404 | 16.04% | 32.29% |
| Moderately suitable | 1,482,357 | 28.73% | 57.85% |
| Marginally suitable | 227,030 | 4.40% | 8.86% |
| Less suitable | 4356 | 0.08% | 0.17% |
| Restricted area | 2,597,721 | 50.34% | / |

### *3.2. Spatial Distribution of Geographic Potential*

Geographic potential in this study is defined as the candidate PV construction space corresponding to the upper two suitability classes (PDSI $\geq$ 3.40), determined after applying the Boolean restrictive exclusion mask. The results indicate that this suitable zone (comprising highly suitable and suitable classes) covers a total area of approximately 0.85 million km$^2$ (accounting for 33.1% of the potential area).

To evaluate the spatial consistency of the assessment results, this study conducted a GIS overlay analysis between the identified suitable zones and the complete dataset of existing PV power stations in 2023 [23]. Quantitative spatial statistics across all 2111 valid centroid sample points reveal that 81.00% (1710 points) fall within the upper two Equal Interval suitability classes (PDSI $\geq$ 3.40, comprising 79.49% Suitable and 1.52% Highly suitable), indicating a high spatial correspondence between this cutoff and existing solar power installations. For cartographic clarity at a macroscopic scale, Figure 6 displays a representative spatial subset of these operational stations overlaid on the suitability map. The geographic potential results were further evaluated using the ROC method described in Section 2.5.1. The model achieved an AUC of 0.792 $\pm$ 0.013 (95% CI: 0.778–0.804, $n$ = 2111 sample points per class, 2000 bootstrap iterations), indicating good discriminatory capacity in identifying existing PV sites (Figure 7).

Furthermore, to observe the sensitivity of the geographic potential to different classification rules, we compared the baseline Equal Interval cutoff (PDSI $\geq$ 3.40, yielding ~0.85 million km$^2$ and 19,069 TWh/year) against an alternative Natural Breaks (Jenks) classification. Adopting the Natural Breaks method shifts the cutoff for the upper two suitability classes upward to PDSI $\geq$ 3.85, which compresses the candidate suitable area to 177,975 km$^2$ (6.7% of the potential area) and reduces the corresponding technical generation potential to ~3873 TWh/year (a ~80% reduction). Because the Natural Breaks threshold ($\geq$3.85) yields a narrower candidate area that omits a substantial proportion of existing operational solar facilities, adopting the Equal Interval cutoff (PDSI $\geq$ 3.40) provides a more inclusive and empirically consistent spatial reference for preliminary regional screening.

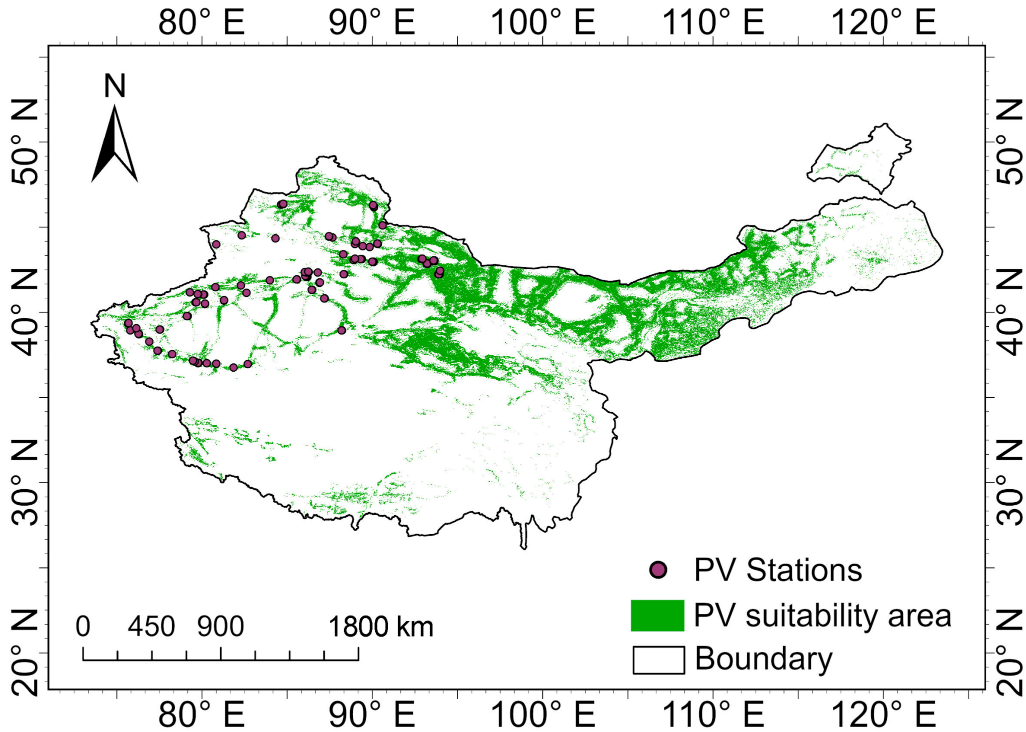


**Figure 6.** Spatial overlap between PV geographic potential areas and existing PV stations. (Note: A representative subset of the existing PV stations is displayed for visualization purposes to maintain cartographic clarity at this macro-regional scale. The full dataset utilized in this study comprises a total of 1923 existing PV stations).

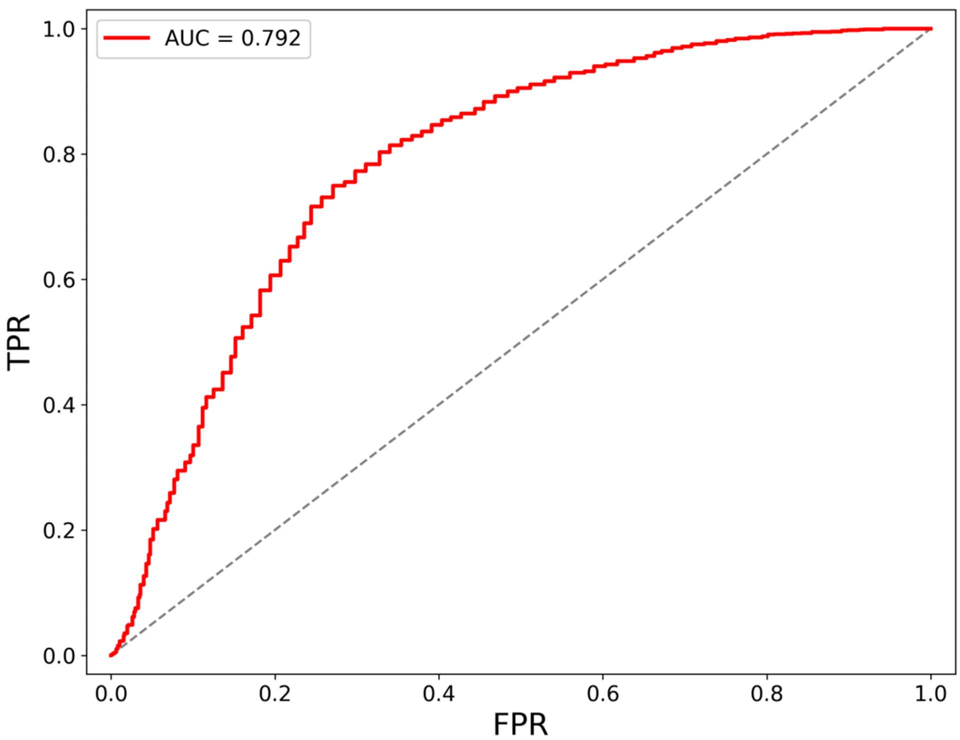


**Figure 7.** ROC of PV suitability area. The grey dashed line represents a random classifier (AUC = 0.5) as a reference baseline.

### *3.3. Estimation Results of Power Generation Potential*

Based on the geographic potential identified in Section 3.2, this study estimated the technical power generation potential of the study area using Equation (5) [45]. At a 30 m resolution, the theoretical annual power generation of a single grid cell ranges between 72,747.3 kWh and 220,318 kWh (Figure 8). It should be explicitly stated that the per-cell values illustrated in Figure 8 represent the raw generation capacity (assuming 100% spatial coverage) before applying the land-utilization reduction. To scale these theoretical pixel values to a realistic regional total, this study conservatively adopted a 10% effective land-utilization factor (to account for necessary module spacing, maintenance access, and terrain shading effects) [52]. Applying this consistent scaling basis, the total scenario-based technical power generation potential of the study area is estimated to be approximately 19,069 TWh. This value must be interpreted as a theoretical upper bound under the baseline scenario, rather than immediately deployable annual generation. Nevertheless, this figure accounts for approximately 207% of China's total societal electricity consumption in 2023 (approximately 9224 TWh) [53], fully demonstrating the strategic support role of this region in safeguarding national energy security.

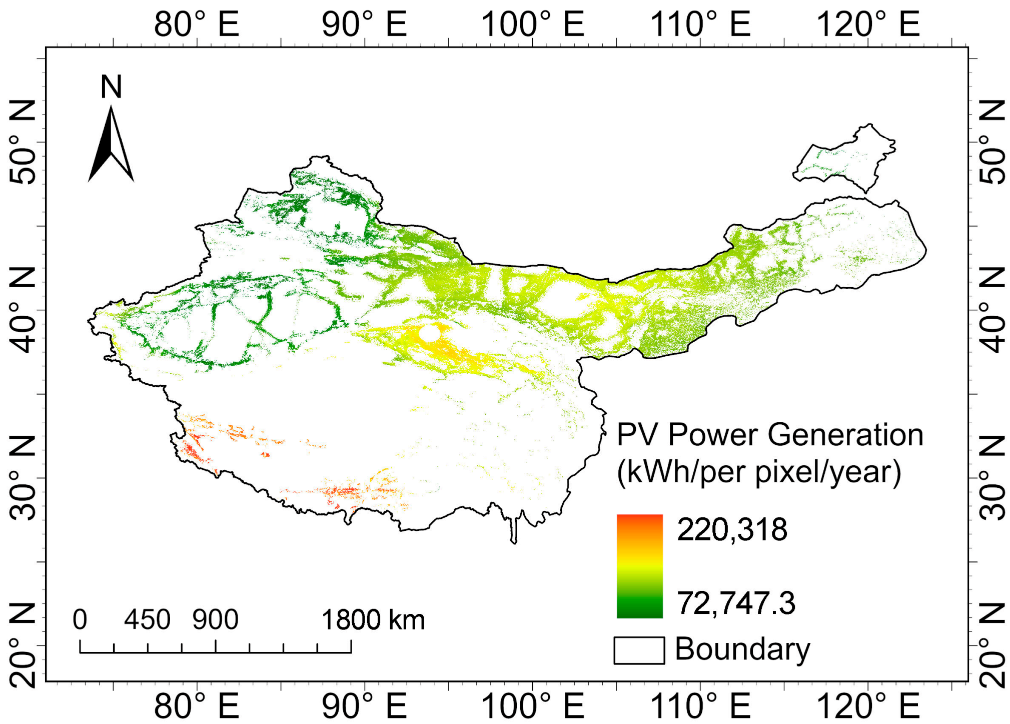


**Figure 8.** Spatial distribution of theoretical technical power generation potential. The map illustrates the annual raw generation capacity per 30 m grid cell (kWh/per pixel/year) within the identified suitable and highly suitable zones, prior to the application of the regional 10% land-utilization scaling factor.

Subsequently, an expanded uncertainty analysis was conducted to evaluate the impact of key modeling assumptions—specifically conversion efficiency (EF), performance ratio (PR), and the land-utilization factor—as these variables directly scale the final estimate. For conversion efficiency, varying the baseline (0.15) from 0.13 to 0.22 yields a scenario-based technical potential ranging from 16,526 TWh to 27,967 TWh; calculations indicate that for every one-percentage-point increase in EF, the regional generation increases by approximately 1271.3 TWh. Similarly, adjusting the baseline PR (70%) to more optimistic scenarios of 80% or 85% proportionally scales the total generation to 21,793 TWh and 23,155 TWh, respectively. Furthermore, the land-utilization factor remains a highly sensitive parameter; if empirical deployment density allows for a 15% utilization rate rather than the conservative 10% baseline, the scenario-based potential would linearly increase to 28,603 TWh, whereas a stricter 5% constraint would halve the baseline estimate to 9534 TWh.

### 3.4. Assessment Results of Carbon Emission Reduction Potential

Based on the power generation potential derived in Section 3.3 and Equation (6) [50], this study estimates the carbon emission reduction potential of PV development in China's arid and semi-arid regions [14] to be 14.65 billion tons of $CO_2$ as a gross theoretical upper bound under complete coal substitution (Figure 9). It is crucial to note that this represents a gross theoretical upper bound. Under a more realistic scenario utilizing current regional grid-emission factors (e.g., approximately 0.5810 t $CO_2$/MWh for Northwest China), the realizable annual abatement would dynamically depend on actual grid integration, transmission capacity, and regional electricity demand. This reduction exceeds the national total carbon emissions reported for 2021 [54], representing a significant strategic contribution toward advancing the national implementation of the "Dual Carbon" goals [2].

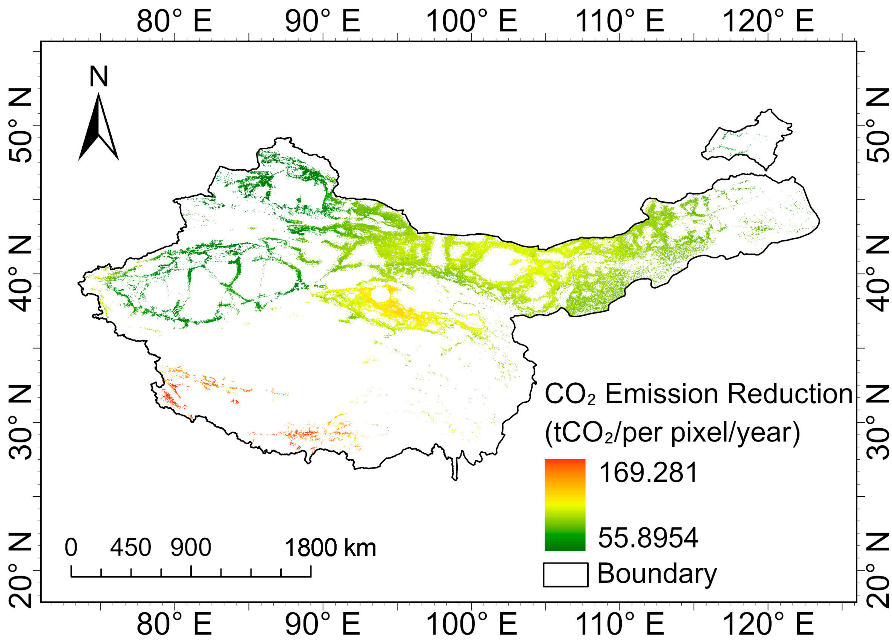


**Figure 9.** Spatial distribution of theoretical carbon emission reduction potential. The map illustrates the estimated gross annual $CO_2$ emission reduction per 30 m grid cell (t $CO_2$/per pixel/year) under a complete coal-substitution scenario within the suitable zones.

From a global perspective, greenhouse gas emission reductions in this magnitude not only help alleviate the pressure of climate warming but also improve the regional microclimate through the shading and evaporation reduction effect of PV facilities, thereby promoting the restoration of fragile ecosystems and control of desertification. In summary, the large-scale deployment of PV power stations in this region represents a scientific pathway to achieve a synergistic pathway that aligns the low-carbon transition of the energy structure with ecological environmental governance.

### 3.5. Sensitivity Analysis of Indicator Weights

Given that the B-BWM intrinsically relies on expert elicitation, validating the robustness of the spatial decision-making model against subjective weight uncertainties is crucial. A comprehensive One-At-a-Time (OAT) [55] sensitivity analysis was conducted by perturbing the weights of the dominant criteria (GHI, Distance to roads, and NDVI) at intervals of ±10%, ±20%, and ±30%. To maintain a sum of 1, the remaining weights were proportionally scaled during each permutation.

It should be noted that the baseline AUC reported in the sensitivity analyses (0.789) exhibits a minor, statistically negligible deviation of 0.003 from the primary validation AUC

(0.792) reported in Section 3.2. This slight variation occurs because the ROC validation and the OAT/LOO sensitivity evaluations were executed as separate, independent computational runs. Due to the stochastic nature of generating pseudo-absence background points within the potential area, slight sample variations naturally arise across distinct runs; however, the sensitivity baseline (0.789) falls well within the 95% confidence interval of the primary bootstrap validation (0.778–0.804), confirming complete statistical and methodological consistency.

As illustrated in Figure 10 and detailed in Table S3, the model exhibits exceptional stability across all weight perturbation intervals (±10%, ±20%, and ±30%). Under a reasonable ±10% perturbation range across all tested indicators, the predictive accuracy (AUC) deviation remained ≤0.013, and the spatial overlap of the suitable areas stayed above 94.8%. Notably, the model revealed an asymmetric response to different constraints (Figure 10a,c). While GHI acts as the sensitivity-limiting factor—where an extreme +30% weight artificially forces a weight squeeze effect that drops spatial overlap to 79.05%—the distance to roads demonstrated a slight positive correlation with AUC when its weight increased. This effectively captures the reality of infrastructure planning, where transport logistics strongly dictate micro-siting preferences in the vast arid regions. Furthermore, the NDVI constraint proved to be extremely robust, with AUC fluctuating by merely 0.4% even under extreme ±30% disturbances.

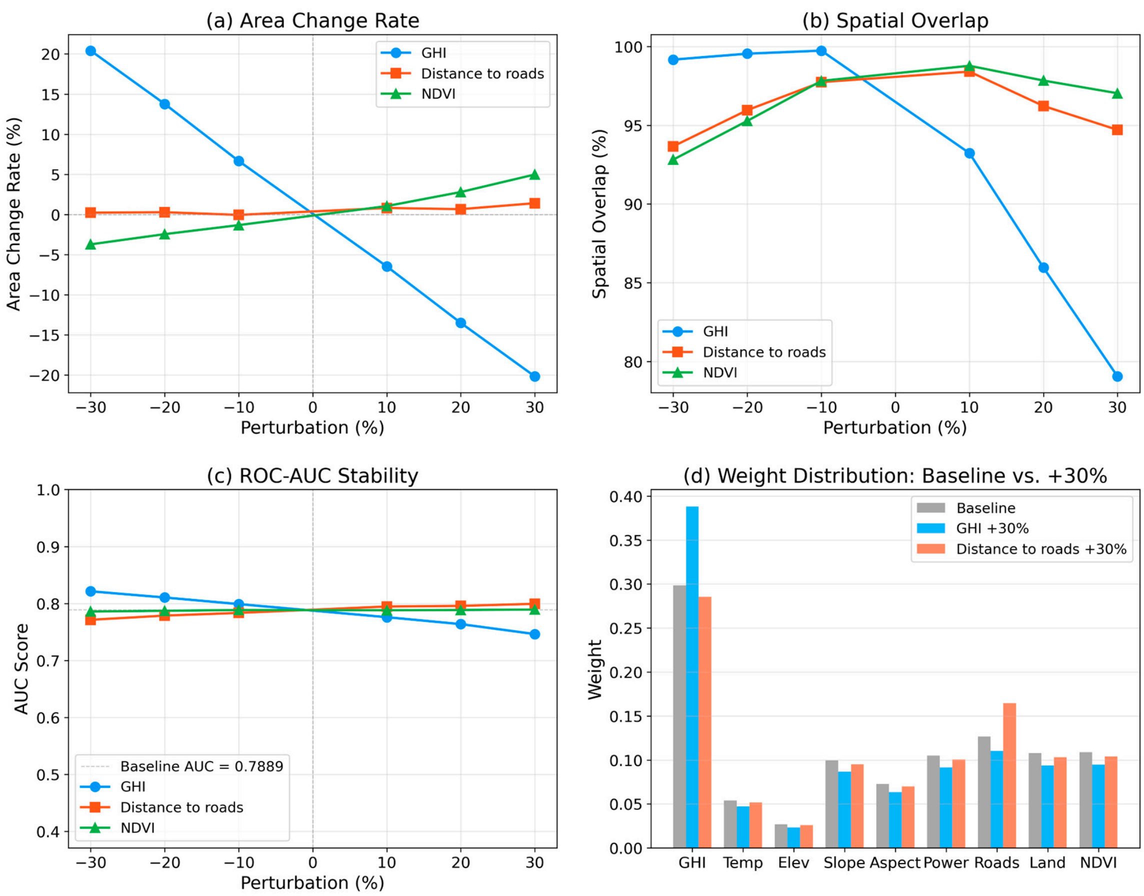


**Figure 10.** Comprehensive OAT sensitivity analysis of the B-BWM weights: (**a**) area change rate; (**b**) spatial overlap of suitable zones; (**c**) ROC-AUC stability; (**d**) weight distribution shifts under extreme perturbations.

Regarding the Leave-One-Out (LOO) [56] sensitivity analysis for NDVI, removing the vegetation criterion resulted in an 8.1% reduction in the total suitable area and an AUC decrease from 0.789 to 0.764 (Δ"AUC" = −0.025). To correctly interpret this result, it is necessary to distinguish the stability of site-specific discrimination from the stability of the mapped area extent. While the relatively stable AUC confirms that discriminating existing PV infrastructure relies primarily on solar and topographic fundamentals rather than redundant vegetation metrics, the contraction in spatial area demonstrates that NDVI exercises a material influence on regional boundary delineation. Therefore, including NDVI acts as an independent micro-ecological filter that restricts development in fragile ecotones at the margins, scientifically justifying its baseline inclusion.

## 4. Discussion

### *4.1. Spatial Heterogeneity and Multi-Resolution Mapping Integration*

Many existing macro-scale assessments of solar resources heavily rely on coarse datasets, typically at resolutions of 1 km or lower [57]. This reliance inherently introduces a smoothing effect, where localized terrain variations and small-scale land-use constraints are averaged out into single pixels. Such generalization masks spatial nuances critical for micro-siting, including narrow transport corridors, fragmented ecological patches, and undulating topography [11]. Variables such as terrain slope and aspect directly dictate the incident solar radiation and installation feasibility, making high-resolution inputs indispensable. By standardizing the evaluation to a 30 m analytical grid integrating mixed-resolution data, the present study provides an effective framework for preliminary regional screening. Importantly, we explicitly recognize that while topographic and land-cover boundaries operate at 30 m, the effective thematic resolution of the integrated output is inherently limited by the native resolution of each input dataset (e.g., 1 km for climatic and vegetation layers). Therefore, our outputs are designed to support regional macro-planning and priority zone identification rather than site-specific operational feasibility assessments.

Unlike previous evaluations constrained by administrative boundaries or generalized indices [13], our spatial outputs delineate the suitability landscape of arid and semi-arid regions with much higher fidelity. The generated maps highlight a distinct geographical pattern characterized by large-scale concentration and small-scale dispersion. Within the core areas of the Qaidam Basin and Alxa Plateau, the flat terrain and vast barren lands create highly contiguous suitable zones. These areas present ideal physical conditions for the centralized development of ultra-large utility-scale photovoltaic bases. Conversely, the margins of the study area, particularly near expanding settlements and interlaced pastoral lands, exhibit fragmented suitability. Such fragmented zones are highly compatible with distributed solar projects, facilitating localized power generation and consumption [9]. This refined spatial segmentation minimizes land-use conflicts and aligns well with the actual coordinates of operational stations, demonstrating superior predictive accuracy over generic models [23].

### *4.2. Robustness and Asymmetric Responses in Spatial Decision-Making*

The OAT sensitivity analysis [55] (Figure 10) not only confirms the overall reliability of the B-BWM weights but also reveals an asymmetric response to different constraints that reflects real-world engineering logic. While GHI acts as the sensitivity-limiting factor—where an extreme +30% weight artificially forces a weight squeeze effect that drops spatial overlap to 79.05%—the distance to roads demonstrated a slight positive correlation with AUC when its weight increased. This captures the reality of infrastructure planning, where transport logistics strongly dictate micro-siting preferences in vast arid regions. These findings confirm that the baseline weighting scheme optimally balances resource endowment with socio-economic and ecological constraints, proving highly resilient to subjective scoring deviations.

Furthermore, a LOO sensitivity analysis [56] confirmed the framework's structural integrity by omitting the NDVI criterion to test for spatial multicollinearity. The recalibrated model yielded a high normalized spatial overlap (86.4%) and robust predictive accuracy (AUC: 0.764, compared to the baseline of 0.789), confirming that the identification of PV infrastructure relies primarily on physical fundamentals rather than redundant vegetation metrics. Meanwhile, the 8.1% contraction in suitable area underscores NDVI's role as an independent micro-ecological filter. It effectively restricts development in fragile ecotones overlooked by discrete land-cover labels, confirming the framework's structural necessity and ecological conservatism.

While the OAT analysis confirms the robustness of the B-BWM weighting scheme, the deterministic Boolean thresholds (e.g., a slope exclusion criterion of 20° and an elevation cutoff of 4500 m) directly dictate the boundary of the potential mask. To quantify the model's sensitivity to these thresholds, a scenario analysis was conducted on the primary topographic constraint (slope). The results indicate that relaxing the slope threshold from 20° to 25° results in an 80.1% increase in the geographic potential area (from 848,672 $km^2$ to 1,528,488 $km^2$), which correspondingly raises the theoretical annual generation potential from 19,069 TWh to 34,344 TWh. This substantial variation indicates that the model output is highly sensitive to the slope parameter. However, incorporating these topographically complex transition zones (20–25°) would significantly escalate civil engineering costs, exacerbate inter-row shading losses, and trigger severe soil erosion risks in fragile arid ecosystems, necessitating specialized and economically prohibitive mountain–PV technologies. Conversely, adopting a much stricter threshold (e.g., 10° or 15°) would force PV deployment exclusively onto absolutely flat terrains, thereby inadvertently intensifying spatial conflicts with high-value agricultural oases and human settlements in arid basins. Therefore, this quantitative result strongly justifies the adoption of the 20° threshold, informed by the principles of standard engineering guidelines (GB 50797-2012) [31] and practical economic constraints. It demonstrates that the baseline setting provides an optimal equilibrium: it maximizes the utilization of undulating marginal lands while avoiding the severe overestimation of realistically deployable capacity in hazardous terrains.

Furthermore, to observe the sensitivity of the assessment results to climatic indicator boundaries, a quantitative sensitivity analysis was conducted on the five-tier temperature scoring intervals. Systematically shifting all breakpoints of the inverted-U temperature classification by $\pm 1$ °C and $\pm 2$ °C resulted in a relative area variation of only −4.58% to +4.70% (overall change < 5%) in the candidate suitable zone (PDSI $\geq$ 3.40), while the spatial discriminatory accuracy against the existing PV stations remained stable ($\Delta$AUC $\leq$ 0.005). This indicates that the spatial delineation of regional priority PV zones is predominantly governed by solar irradiance (GHI) and topographic constraints, and is insensitive to minor shifts in temperature scoring thresholds.

### *4.3. Synergies Between Solar Deployment and Ecological Restoration*

Deploying renewable energy infrastructure in arid regions presents unique opportunities to harmonize resource extraction with environmental restoration. The proposed evaluation framework operates on a strict exclusion-first logic, establishing rigid spatial boundaries to safeguard vulnerable ecosystems. By comprehensively omitting nature reserves, mapped farmland proxies [37], and critical watersheds from the candidate area, the model intrinsically prevents solar development from encroaching upon mapped ecological assets or arable land proxies. We explicitly note that OpenStreetMap farmland layers serve as an analytical screening proxy rather than a statutory legal boundary.

Targeting marginal lands such as the Gobi desert, sandy wastelands, and areas with sparse vegetation for photovoltaic installations provides significant ecological co-benefits.

Once constructed, solar arrays alter the local microclimate beneath and around the modules. The physical presence of the panels provides extensive shading, which effectively reduces direct solar radiation reaching the ground. This shading mechanism lowers local soil temperatures and substantially curtails soil moisture evaporation. Concurrently, the module arrays act as aerodynamic barriers, decreasing near-surface wind speeds and mitigating wind-driven soil erosion [38]. Because our GIS-based suitability framework does not explicitly simulate soil moisture, wind erosion, vegetation succession, or hydrological responses, these ecological advantages should be interpreted as possible site-specific co-benefits documented in previous field studies rather than direct numerical outputs of the present model. As observed in operational desert PV facilities, microclimatic modifications could potentially facilitate the natural recovery of drought-resistant vegetation over time, highlighting an opportunity to align renewable deployment with regional ecological preservation. Such an integrated approach to land use transforms solar farms from single-purpose energy facilities into active components of regional ecological governance, supporting national emission reduction targets and broader climate change mitigation strategies [2,5].

### 4.4. Evaluation of Generation Potential and Energy Security

The geospatial analysis indicates that the identified suitable and highly suitable areas hold an annual technical generation potential of approximately 19,069 TWh. To contextualize the magnitude of this capacity, it corresponds to approximately 207% of the total societal electricity consumption recorded in China during 2023 [53]. The sheer volume of this harvestable solar energy underscores the irreplaceable strategic position of the northwestern arid regions in stabilizing the national energy supply. This immense renewable capacity is not merely a theoretical construct but a foundational element required to decarbonize heavily industrialized economies reliant on coal-fired generation.

When evaluated against comparable multi-criteria decision-making models [45], the capacity estimates derived in this study remain notably conservative. This restraint is deliberate and stems from the integration of an effective land utilization rate of 10 percent [52]. Setting the utilization threshold at this level accounts for the practical spatial requirements of large-scale solar arrays, including necessary module spacing to prevent inter-row shading, maintenance access roads, inverter stations, and internal power collection networks. Additionally, the conservative metric absorbs potential losses associated with unfavorable micro-terrain shading that even a 30 m resolution might not fully resolve. By grounding the theoretical potential in operational realities, the findings offer a highly reliable baseline for grid planners and policymakers coordinating long-distance power transmission corridors.

### 4.5. Methodological Limitations and Future Research Directions

Despite the precision gained through high-resolution spatial datasets and multi-dimensional indicators, the current assessment framework retains certain analytical limitations that warrant further investigation. Primarily, the model focuses on the geographic and technical suitability of the operational phase, omitting a comprehensive life cycle assessment of the solar infrastructure. Future studies should integrate the embodied carbon emissions generated during the extraction of raw materials, the manufacturing of silicon wafers, and the eventual decommissioning and recycling of photovoltaic panels [41]. Quantifying the actual energy payback time alongside short-term construction disturbances to the soil profile could temporarily destabilize the surface. Furthermore, the linear arrangement of PV arrays and associated access roads may contribute to habitat fragmentation, particularly in areas serving as wildlife corridors, potentially disrupting the movement of terrestrial species. The large-scale impervious surfaces and land grading required for PV installation may also alter natural surface runoff patterns, affecting local hydrological regimes in endorheic basins. Additionally, the water requirements for periodic panel cleaning—estimated at approximately 0.5 to 1.0 L/m$^2$ per cleaning cycle—represent a non-trivial demand in water-scarce arid regions, potentially competing with local ecological and agricultural water use. These potential adverse effects warrant careful site-level environmental impact assessment and the adoption of mitigation measures such as wildlife-friendly fencing, micro-topography-preserving construction techniques, and dry-cleaning or robotic cleaning technologies to minimize water consumption would provide a more holistic metric of environmental sustainability.

Another critical gap is the exclusion of localized economic variables and grid topology. The optimal generation zones identified are geographically remote from the primary industrial load centers. Therefore, spatial distance parameters should ideally be coupled with specific cost–benefit analyses detailing high-voltage transmission construction costs and corresponding line losses over long distances [44].

Methodologically, the utilization of the Bayesian Best–Worst Method successfully mitigated subjective inconsistencies compared to conventional hierarchical processes [16]. Nevertheless, prioritizing indicators still heavily relies on expert elicitation, which inevitably introduces residual subjectivity into the evaluation weighting, especially when balancing ecological sensitivity against technical efficiency. Furthermore, the temporal mismatch among the 2020 land-cover dataset, 2023 PV sites, and recent infrastructure data introduces minor spatial uncertainties, particularly in rapidly urbanizing transition zones. To enhance the robustness of future siting models, researchers should consider cross-validating expert weights with global sensitivity analyses, such as Morris screening [58], to systematically isolate the influence of individual spatial constraints. Most importantly, transitioning towards data-driven machine learning algorithms (such as the Random Forest method, which establishes non-linear, data-driven objective weights rather than relying on purely subjective elicitations) trained on the precise coordinates of existing power plants will be essential. Such advancements will significantly reduce human bias, thereby refining the precision and universal applicability of the decision-making framework.

Furthermore, while bootstrap resampling (2000 iterations) evaluated the statistical stability of our ROC/AUC assessment against background sample variance, it does not provide strict spatial independence. Because existing PV stations often cluster along transmission corridors or desert basins, spatial autocorrelation among neighboring sites could introduce slight optimism into the reported AUC metrics. The absence of a spatially blocked cross-validation scheme remains an analytical limitation of this study, which should be addressed in future research to better test regional model transferability.

## 5. Conclusions

This study presents a multi-dimensional, multi-resolution integrated framework for evaluating PV development suitability in the arid and semi-arid regions of China. By integrating Boolean logic, the B-BWM, and Equal Interval classification, the framework demonstrates practical utility for preliminary regional screening on a 30 m analytical grid integrating mixed-resolution data. We emphasize that while topographic and land-cover boundaries are delineated at 30 m, the effective thematic resolution of the final suitability maps is inherently limited by the native resolution of each input dataset. The applied exclusion first, suitability later logic avoids encroachment on known sensitive ecological spaces and mapped farmland proxies, while the integrated evaluation model achieved a high predictive accuracy with an AUC of 0.79, proving to be a robust tool for identifying optimal PV sites in complex and sensitive terrains. Using this framework, we revealed immense development potential across 0.85 million km$^2$ of candidate PV construction space (PDSI $\geq$ 3.40), characterized by a spatial pattern of large-scale concentration and small-scale dispersion. The assessment indicates an annual technical generation potential of 19,069 TWh, which can offset approximately 14.65 billion tons of $CO_2$ emissions annually. Furthermore, this evaluation demonstrates potential applications for synergizing massive renewable energy transition with ecosystem preservation, providing a critical methodological benchmark for global renewable planning on marginal lands and directly contributing to the achievement of China's "Dual Carbon" goals. Although limited by the exclusion of economic variables and full-lifecycle ecological impacts, future research integrating cost–benefit analyses and machine learning will further enhance the framework's commercial viability and global applicability.

**Supplementary Materials:** The following supporting information can be downloaded at: https://www.mdpi.com/article/10.3390/su18168218/s1. Table S1: Priority classification of the evaluation criteria; Table S2: Criteria weights from B-BWM; Table S3 Numerical summary of One-At-a-Time (OAT) weight perturbations and corresponding model sensitivity metrics across all tested scenarios.

**Author Contributions:** Conceptualization, C.W. and Z.S.; methodology, C.W. and Z.S.; software, C.W.; validation, C.W. and Z.S. and Q.Y.; formal analysis, C.W. and Z.S.; investigation, C.W. and Z.S. and Q.Y.; resources, Q.Y.; data curation, Y.G. and S.X. and Y.L.; writing—original draft preparation, C.W. and Z.S.; writing—review and editing, Q.Y.; visualization, C.W. and Z.S. and D.L.; supervision, Q.Y.; project administration, Q.Y.; funding acquisition, Q.Y. All authors have read and agreed to the published version of the manuscript.

**Funding:** This work was supported by the National College Student Innovation and Entrepreneurship Training Program #1 under Grant No. 202410755006, Investigation and Evaluation of the Impact of Energy and Mineral Resources Development on the Regional Ecological Environment in the Turpan Basin #2 under Grant No. 2021xjkk1104, and "Tianchi Talent" Young Doctor Program of Xinjiang Uygur Autonomous Region.

**Institutional Review Board Statement:** Not applicable.

**Informed Consent Statement:** Not applicable.

**Data Availability Statement:** The datasets for roads, railways, nature reserves, water bodies, wetlands, farmlands, forests, and powerlines are available under the OpenStreetMap license at https://www.openstreetmap.org/ [21] (accessed on 17 October 2025). The PV power plant spatial data is available in Gao et al. [23]. The boundary of the arid and semi-arid regions is derived from Zhai et al. [14]. The Global Horizontal Irradiance (GHI) data was obtained from the Global Solar Atlas [18]. The settlement data is available at GHSL-based Chinese urban entities (1975–2020) [24]. Topographic data, including aspect, slope, and elevation, was extracted from the SRTM DEM via the GEE platform [17]. The temperature data was acquired from MODIS products via the GEE platform [25]. The land use dataset is available in Liu et al. [25], and the NDVI data was sourced from the MOD13A3 MODIS product via NASA [20].

**Acknowledgments:** The authors would like to thank all contributors for their valuable contributions to this work. During the preparation of this manuscript, the authors used Gemini 3.1 for the purposes of language polishing. The authors have reviewed and edited the output and take full responsibility for the content of this publication.

**Conflicts of Interest:** The authors declare no conflicts of interest.

## Abbreviations

The following abbreviations are used in this manuscript:

| | |
|---|---|
| AHP | Analytic hierarchy process |
| ARIMA | AutoRegressive integrated moving average |
| AUC | Area under the curve |
| B-BWM | Bayesian best–worst method |

| | |
|---|---|
| CE | Carbon emission reduction |
| CGCS2000 | China Geodetic Coordinate System 2000 |
| CI | Confidence interval |
| CR | Consistency ratio |
| CUMT | China University of Mining and Technology |
| DEM | Digital elevation model |
| DMs | Decision-makers |
| EF | Efficiency with which the PV system converts solar energy into electrical energy |
| EPSG | European Petroleum Survey Group |
| FN | False negative (points that are truly PV areas but not classified as suitable) |
| FP | False positive (points that are truly not PV areas but classified as suitable) |
| FPR | False positive rate |
| FPV | Floating PV |
| GaAs | Gallium arsenide |
| GEE | Google Earth Engine |
| GHI | Global horizontal irradiance |
| GIS | Geographic information systems |
| IEA | International Energy Agency |
| IPCC | Intergovernmental Panel on Climate Change |
| LOO | Leave-one-out |
| LST | Land surface temperature |
| MCDM | Multi-criteria decision-making |
| MODIS | Moderate resolution imaging spectroradiometer |
| NASA | National Aeronautics and Space Administration |
| NDVI | Normalized difference vegetation index |
| NEA | National Energy Administration |
| NGCC | National Geomatics Center of China |
| O&M | Operation and maintenance |
| OAT | One-at-a-time |
| OSM | OpenStreetMap |
| PDSI | Photovoltaic development suitability index |
| POA | Plane-of-array |
| PR | Performance ratio |
| PV | Photovoltaic |
| ROC | Receiver operating characteristic |
| SEM | Structural equation modeling |
| SRTM | Shuttle radar topography mission |
| TN | True negative |
| TOPSIS | Technique for order preference by similarity to ideal solution |
| TP | True positive |
| TPR | True positive rate |
| TPSE | Total photovoltaic solar energy |
| WLC | Weighted linear combination |

## References


1. IPCC. *Climate Change 2022: Mitigation of Climate Change*; Contribution of Working Group III to the Sixth Assessment Report of the Intergovernmental Panel on Climate Change; Cambridge University Press: Cambridge, UK; New York, NY, USA, 2022. [CrossRef]
2. Central Committee of the Communist Party of China; State Council of the People's Republic of China. Opinions on Fully, Accurately, and Comprehensively Implementing the New Development Concept and Doing a Good Job in Carbon Peaking and Carbon Neutrality. Beijing. 2021. Available online: https://www.mofcom.gov.cn/zcfb/zgdwjjmywg/art/2021/art_dee4aa25a54049d1bd69b6cfff7d195d.html (accessed on 10 July 2026).
3. IEA. *World Energy Outlook 2023*; International Energy Agency: Paris, France, 2023. Available online: https://www.iea.org/reports/world-energy-outlook-2023 (accessed on 10 July 2026).

4. Institute for Carbon Neutrality. *2023 Global Carbon Neutrality Annual Progress Report*; Tsinghua University: Beijing, China, 2023. Available online: https://www.icon.tsinghua.edu.cn/en/info/1068/1066.htm (accessed on 10 July 2026).
5. Zou, C.; Xiong, B.; Xue, H.; Zheng, D.; Ge, Z.; Wang, Y.; Jiang, L.; Pan, S.; Wu, S. The role of new energy in carbon neutrality. *Pet. Explor. Dev.* **2021**, *48*, 480–491. [CrossRef]
6. China Meteorological Administration. 2023 Annual Bulletin of China's Wind and Solar Energy Resources. Beijing. 2024. Available online: https://www.cma.gov.cn/zfxxgk/gknr/qxbg/202402/t20240222_6082082.html (accessed on 10 July 2026).
7. National Energy Administration. Construction Status of Photovoltaic Power Generation in 2023. Beijing. 2024. Available online: https://www.nea.gov.cn/2024-02/28/c_1310765696.htm (accessed on 10 July 2026).
8. National Energy Administration. Monitoring and Evaluation Results of National Renewable Energy Power Development in 2023. Beijing. 2024. Available online: https://zfxxgk.nea.gov.cn/2024-10/10/c_1310787115.htm (accessed on 10 July 2026).
9. Yang, H.; Xu, Y.; Zhou, K.; Li, J. Mapping development potential and priority zones for utility-scale photovoltaic on the Qinghai-Tibet Plateau. *Renew. Energy* **2024**, *237*, 121546. [CrossRef]
10. Zhao, Y.; Li, S.; Yang, D.; Yahaya, I.I.; Pan, H. Assessment of site suitability for centralized photovoltaic power stations in Northwest China's six provinces. *J. Environ. Manag.* **2024**, *366*, 121820. [CrossRef] [PubMed]
11. Noorollahi, Y.; Ghenaatpisheh Senani, A.; Fadaei, A.; Simaee, M.; Moltames, R. A framework for GIS-based site selection and technical potential evaluation of PV solar farm using Fuzzy-Boolean logic and AHP multi-criteria decision-making approach. *Renew. Energy* **2022**, *186*, 89–104. [CrossRef]
12. Zhou, J.; Ding, Q.; Zou, Z.; Deng, J.; Xu, C.; Yang, W. Land suitability evaluation of large-scale photovoltaic plants using structural equation models. *Resour. Conserv. Recycl.* **2023**, *198*, 107179. [CrossRef]
13. Liang, L.; Chen, Z.; Chen, S.; Zheng, X. Evaluation of Site Suitability for Photovoltaic Power Plants in the Beijing–Tianjin–Hebei Region of China Using a Combined Weighting Method. *Land* **2023**, *13*, 40. [CrossRef]
14. Zhai, J.; Su, B.; Krysanova, V.; Vetter, T.; Gao, C.; Jiang, T. Drought evolution, severity and trends in mainland China over 1961–2013. *Sci. Total Environ.* **2017**, *590–591*, 1113–1122. [CrossRef] [PubMed]
15. Zhu, Y.; Chen, Y.; Ren, L.; Lü, H.; Zhao, W.; Yuan, F.; Xu, M. Ecosystem restoration and conservation in the arid inland river basins of Northwest China: Problems and strategies. *Ecol. Eng.* **2016**, *94*, 629–637. [CrossRef]
16. Mohammadi, M.; Rezaei, J. Bayesian Best-Worst Method: A probabilistic group decision making model. *Omega* **2020**, *96*, 102075. [CrossRef]
17. U.S. Geological Survey (USGS). Shuttle Radar Topography Mission (SRTM) Global 1 Arc Second Version 3 (SRTMGL1_003). 2000. Available online: https://earthexplorer.usgs.gov/ (accessed on 17 October 2025).
18. Global Solar Atlas. Global Horizontal Irradiation (GHI) Data. 2024. Available online: https://globalsolaratlas.info/ (accessed on 10 July 2026).
19. NASA LP DAAC. *MODIS/Terra Land Surface Temperature/Emissivity 8-Day L3 Global 1km (MOD11A2)*; NASA LP DAAC: Sioux Falls, SD, USA, 2021. [CrossRef]
20. National Aeronautics and Space Administration (NASA). *MOD13A3 MODIS/Terra Vegetation Indices Monthly L3 Global 1 km SIN Grid*; NASA: Washington, DC, USA, 2015. [CrossRef]
21. OpenStreetMap Contributors. 2025. Available online: https://www.openstreetmap.org (accessed on 17 October 2025).
22. Arderne, C.; Zorn, C.; Nicolas, C.; Koks, E.E. Predictive mapping of the global power system using open data. *Sci. Data* **2020**, *7*, 19. [CrossRef] [PubMed]
23. Gao, Y.; Yang, Q.; Chang, P.; Wang, C.; Wang, X.; Yu, M.; Liu, R.; Dilixiati, B.; Shi, Q.; Zhakypbek, Y. Assessment of the Spatiotemporal Patterns and Ecological Impacts of Photovoltaic Power Plants in Central Asia. *Earth's Future* **2026**, *14*, e2025EF006335. [CrossRef]
24. Han, J.; Hu, Z.; Zhou, K. *GHSL-Based Chinese Urban Entities (1975–2020)*; Science Data Bank: Beijing, China, 2024. [CrossRef]
25. Liu, L.; Zhang, X. *2020 Global 30m Surface Coverage Fine Classification Products*; Aerospace Information Research Institute, Chinese Academy of Sciences: Beijing, China, 2021. [CrossRef]
26. Malczewski, J. On the use of weighted linear combination method in GIS: Common pitfalls and source of errors. *Trans. GIS* **2000**, *4*, 5–22. [CrossRef]
27. Pontius, R.G.; Schneider, L. Land-cover change model validation by an ROC method for the Ipswich watershed, Massachusetts, USA. *Agric. Ecosyst. Environ.* **2001**, *85*, 239–248. [CrossRef]
28. *GB/T 37526-2019*; Assessment Methods for Solar Energy Resources. State Market Regulatory Administration: Beijing, China, 2019. Available online: https://openstd.samr.gov.cn/bzgk/std/newGbInfo?hcno=B85AFB98947334123364272E950E77DD (accessed on 10 July 2026).
29. *GB/T 39854-2021*; Technical Specification for Performance Evaluation of Photovoltaic Power Plants. State Market Regulatory Administration: Beijing, China, 2021. Available online: https://openstd.samr.gov.cn/bzgk/std/newGbInfo?hcno=A9D2FF863C22D770260742D71F98F43A (accessed on 10 July 2026).

30. *GB/T 42766-2023*; Specification for Evaluation of Solar Energy Resources in Photovoltaic Power Generation. State Market Regulatory Administration: Beijing, China, 2023. Available online: https://openstd.samr.gov.cn/bzgk/std/newGbInfo?hcno=0B24D74EFBD453751DF9915714D44D1B (accessed on 10 July 2026).
31. *GB 50797-2012*; Standard for Design of Photovoltaic Power Station. Ministry of Housing and Urban-Rural Development: Beijing, China, 2012. Available online: https://www.mohurd.gov.cn/gongkai/zc/wjk/art/2024/art_96bd1b03e8d54760b4dff9ad60352ddc.html (accessed on 10 July 2026).
32. Uyan, M. GIS-based solar farms site selection using analytic hierarchy process (AHP) in Karapinar region, Konya/Turkey. *Renew. Sustain. Energy Rev.* **2013**, *28*, 11–17. [CrossRef]
33. International Finance Corporation (IFC). *Utility-Scale Solar Photovoltaic Power Plants: A Project Developer's Guide*; World Bank Group: Washington, DC, USA, 2015. Available online: https://documents.worldbank.org/en/publication/documents-reports/documentdetail/690161467992462412 (accessed on 10 July 2026).
34. State Council of the People's Republic of China. Regulations on the Safety Protection of Highways (Decree No. 593). 2011. Available online: https://www.gov.cn/flfg/2011-03/14/content_1824538.htm (accessed on 10 July 2026).
35. State Council of the People's Republic of China. Regulations on the Safety Management of Railways (Decree No. 639). 2013. Available online: https://www.gov.cn/flfg/2013-09/06/content_2482653.htm (accessed on 10 July 2026).
36. Sanchez-Lozano, J.M.; Teruel-Solano, J.; Soto-Elvira, P.L.; Garcia-Cascales, M.S. Geographical Information Systems (GIS) and Multi-Criteria Decision Making (MCDM) methods for the evaluation of solar farms locations: Case study in south-eastern Spain. *Renew. Sustain. Energy Rev.* **2013**, *24*, 544–556. [CrossRef]
37. Ministry of Natural Resources of the People's Republic of China. Measures for the Administration of Permanent Prime Farmland Protection Red Line. 2025. Available online: https://www.moj.gov.cn/pub/sfbgw/flfggz/flfggzbmgz/202512/t20251218_529533.html (accessed on 10 July 2026).
38. Skoplaki, E.; Palyvos, J.A. On the temperature dependence of photovoltaic module electrical performance: A review of efficiency/power correlations. *Sol. Energy* **2009**, *83*, 614–624. [CrossRef]
39. Dubey, S.; Sarvaiya, J.; Seshadri, B. Temperature Dependent Photovoltaic (PV) Efficiency and Its Effect on PV Production in the World—A Review. *Energy Procedia* **2013**, *33*, 311–321. [CrossRef]
40. Zoghi, M.; Ehsani, A.H.; Sadat, M.; Amiri, M.J.; Karimi, S. Optimization solar site selection by fuzzy logic model and weighted linear combination method in arid and semi-arid region: A case study Isfahan-IRAN. *Renew. Sustain. Energy Rev.* **2017**, *68*, 986–996. [CrossRef]
41. Chang, R.; Yan, Y.; Wu, J.; Wang, Y.; Gao, X. Projected PV plants in China Gobi Deserts would result in lower evaporation and wind. *Sol. Energy* **2023**, *256*, 140–150. [CrossRef]
42. Al Garni, H.Z.; Awasthi, A. Solar PV power plant site selection using a GIS-AHP based approach with application in Saudi Arabia. *Appl. Energy* **2017**, *206*, 1225–1240. [CrossRef]
43. Doorga, J.R.S.; Rughooputh, S.D.D.V.; Boojhawon, R. Multi-criteria GIS-based modelling technique for identifying potential solar farm sites: A case study in Mauritius. *Renew. Energy* **2019**, *133*, 1201–1219. [CrossRef]
44. Fathabadi, H. Impact of high-voltage power transmission lines on photovoltaic power production. *Sol. Energy* **2018**, *163*, 78–83. [CrossRef]
45. Sun, L.; Jiang, Y.; Guo, Q.; Ji, L.; Xie, Y.; Qiao, Q.; Huang, G.; Xiao, K. A GIS-based multi-criteria decision making method for the potential assessment and suitable sites se-lection of PV and CSP plants. *Resour. Conserv. Recycl.* **2021**, *168*, 105306. [CrossRef]
46. Razykov, T.M.; Ferekides, C.S.; Morel, D.; Stefanakos, E.; Ullal, H.; Upadhyaya, H. Solar photovoltaic electricity: Current status and future prospects. *Sol. Energy* **2011**, *85*, 1580–1608. [CrossRef]
47. Tyagi, V.; Rahim, N.A.; Abd Rahim, N.; Selvaraj, J. Progress in solar PV technology: Research and achievement. *Renew. Sustain. Energy Rev.* **2013**, *20*, 443–461. [CrossRef]
48. Chowdhury, M.S.; Shahahmadi, S.A.; Chelvanathan, P.; Tiong, S.K.; Amin, N.; Techato, K.; Nuthammachot, N.; Chowdhury, T.; Suklueng, M. Effect of deep-level defect density of the absorber layer and n/i interface in perovskite solar cells by SCAPS-1D. *Results Phys.* **2020**, *16*, 102839. [CrossRef]
49. Ghasemi, G.; Noorollahi, Y.; Alavi, H.; Shahbazi, M. Theoretical and technical potential evaluation of solar power generation in Iran. *Renew. Energy* **2019**, *138*, 1250–1261. [CrossRef]
50. He, J.; Wang, S.; Zhong, B.; Zhang, Q. Photovoltaic power generation spatial planning and carbon emission reduction benefit assessment based on integrated model: A case study of Qinghai province. *Front. Environ. Sci.* **2025**, *13*, 1658113. [CrossRef]
51. China Electricity Council. *Annual Development Report of China's Electric Power Industry, 2021*; China Building Materials Industry Press: Beijing, China, 2021. Available online: https://www.cec.org.cn/upload/zt/fzbgzt2021/zt2021/index.html (accessed on 10 July 2026).
52. Vermeer, D. Towards More Precise Estimates of Land-Use Requirements for Solar Photovoltaic Power Plants. In *Proceedings of the ISES Solar World Congress*; ISES: Melbourne, Australia, 2021. [CrossRef]

53. National Energy Administration (NEA). National Electricity Industry Statistics for 2023. 2024. Available online: https://www.nea.gov.cn/2024-01/18/c_1310760885.htm (accessed on 10 July 2026).
54. International Energy Agency (IEA). Global Energy Review: $CO_2$ Emissions in 2021. 2022. Available online: https://www.iea.org/reports/global-energy-review-co2-emissions-in-2021 (accessed on 10 July 2026).
55. Chen, Y.; Yu, J.; Khan, S. The spatial framework for weight sensitivity analysis in AHP-based multi-criteria decision making. *Environ. Model. Softw.* **2013**, *48*, 129–140. [CrossRef]
56. Magnusson, M.; Vehtari, A.; Jonasson, J.; Andersen, M. Leave-One-Out Cross-Validation for Bayesian Model Comparison in Large Data. In *Proceedings of the Twenty Third International Conference on Artificial Intelligence and Statistics, Proceedings of Machine Learning Research*; JMLR: Norfolk, MA, USA, 2020; Volume 108, pp. 341–351. Available online: https://proceedings.mlr.press/v108/magnusson20a.html (accessed on 10 July 2026).
57. Wilcox, S.; Gueymard, C. Spatial and temporal variability of the solar resource in the United States. In Proceedings of the 39th ASES National Solar Conference 2010, SOLAR 2010, Phoenix, AZ, USA, 17–22 May 2010; Volume 2.
58. Morris, M.D. Factorial sampling plans for preliminary computational experiments. *Technometrics* **1991**, *33*, 161–174. [CrossRef]




https://doi.org/10.3390/su18168218